Title

Shallow elasticity structure from colocated pressure and seismic stations in the Piñon Flat Observatory and estimation of Vs30

Journal

Geophysical Journal International, 222(1)

ISSN

0956-540X

Authors

Tanimoto, Toshiro
Wang, Jiong

Publication Date

2020-07-01

DOI

10.1093/gji/ggaa195

Peer reviewed

submitted to *Geophys. J. Int.*

Shallow Elasticity Structure from Colocated Pressure and Seismic Stations in the Piñon Flat Observatory and Estimation of Vs30

Toshiro Tanimoto and Jiong Wang

Earth Research Institute and Department of Earth Science, University of California, Santa Barbara, California 93106, USA

SUMMARY

An algorithm developed in Tanimoto and Wang (2019) for deriving shallow elasticity structure from colocated pressure and seismic instruments is applied to data at nine stations in the Piñon Flat Observatory (PFO) in Southern California. Depth resolution kernels indicate that this approach can recover near-surface shear-modulus structure in the upper 50-100 m of the Earth. Our estimate for Vs30 at the closest station (BPH01) agrees with an independent result by Yong et al. (2016) which was based on an active source survey with a geophone array. Vs30 derived from the borehole S-wave speed model by Fletcher et al. (1990) also agrees with estimates at nearby locations, considering the size of uncertainties. Derived structures are much smoother than their models, however. This is because our method analyzes slow quasi-static deformation of the solid Earth in the frequency range 0.005-0.05 Hz that inherently limits depth resolution. Lack of detailed variations in structures does not seem to be the problem for estimating Vs30 as Vs30 is an averaged quantity from the upper 30 m of the Earth. Also our estimates are not affected by different choices of frequency range in the inversion. However, our method may have some difficulty at stiff, hard-rock sites because ground deformation caused by surface pressure can become small and the key observables in our method, the ratios between seismic amplitude and surface pressure change, become difficult to measure accurately.

Key words: Seismic noise – Site effects – Crustal imaging – Structure of the Earth

1 INTRODUCTION

We have recently developed an algorithm to derive shallow elasticity structure from colocated pressure and seismic data (Tanimoto and Wang, 2019). Hereafter, we refer to this paper as Paper 1. One of the useful results that can be obtained by this approach is an independent estimate for Vs30 which is the average S-wave speed in the upper 30 m of the crust (Wald and Allen, 2007; Allen and Wald, 2009). Vs30 is an important parameter for ground-motion prediction as ground-motion amplification can become quite large if near-surface seismic-wave speeds are low (e.g., Shearer and Orcutt, 1987). It is included as a critical parameter in most ground-motion prediction equations (Boore et al., 1997) such as NGA West2 (Bozorgnia, 2014) and NGA East (Goulet et al., 2017).

Estimates for Vs30 have been made by various methods; drilling boreholes is the most direct approach but because of its high cost, non-invasive methods using surface seismic measurements, relying on active as well as passive seismic sources, are often used (e.g., Yong et al., 2016). There are other approaches such as particle motion analysis of body waves (e.g., Zalachoris et al., 2017; Park and Ishii, 2018). Our approach is also an alternative approach that requires colocated pressure and seismic sensors, relying on ambient seismic noise generated by atmospheric processes, primarily through surface pressure changes (Tanimoto and Wang, 2018, 2019). The method has been applied to data from the EarthScope Transportable Array (Tytell et al., 2016, hereafter TA)) but since it is a relatively new technique, it requires further tests before it can join other established techniques that are currently used to estimate Vs30.

The principal aim of this paper is to apply this method to colocated pressure and seismic stations in the Piñon Flat Observatory in Southern California; we compare our results against a carefully estimated Vs30 by Yong et al. (2016) which was mostly based on geophone array data. We also obtained an estimate of Vs30 at the borehole site (Fletcher et al., 1990), based on their S-wave speed model, and compare it to our inversion results. In this comparison process, we will point out the main characteristics of our approach; for example, our approach can derive shear-modulus structures for the upper 50-100 m of the Earth. This is in contrast to other techniques, most of which determine P-wave and S-wave speeds near the surface. In order to compare our method to these studies, we need density structures. For this purpose, we use some empirical relations, developed by Brocher (2005) and Boore (2016).

This paper proceeds in the following order. In section 2, we discuss the Piñon Flat Observatory and the nature of data from nine colocated pressure and seismic sensors. In section 3, we discuss our method, including its basic principles and an example of its application to one of the stations (BPH11) in detail. The critical step is the measurement of the ratios between seismic power spectral density (seismic PSD) and pressure power spectral density (pressure PSD) from colocated seismic and

pressure data. Coherence between seismic and pressure data plays an important role in data selection and determination of the PSD ratios between them. In section 4, we present results for all stations and discuss some characteristic features of our inversion method. One of the most important results is comparison of our results to the USGS study (Yong et al., 2016). We find that our Vs30 value agrees well with their estimate but our structure is much smoother than their structures. We confirm from the depth resolution kernels that our method recovers an averaged, smooth shear-modulus structure approximately in the upper 50 m of the Earth. Despite the lack of details in an inverted structure, our estimates for Vs30 are still close to Yong et al. (2016) at nearby stations. This is most likely because Vs30 is an averaged quantity from the upper 30m of the Earth. In section 5, we summarize our conclusions.

2 DATA

2.1 The Piñon Flat Observatory

Among many different instruments at the Piñon Flat Observatory, we analyze nine colocated stations with pressure and seismic sensors that have similar observational set-up with the EarthScope TA (Tytell et al., 2016; UC San Diego, 2014).

The area of the Piñon FlatObservatory is indicated by a rectangular region in Figure 1. It is roughly 12 km^2 in area, bounded by the Asbestos Mountain to the north, deep canyon to the east, Santa Rosa Mountain to the south, and the Palm Canyon to the west. A summary of geology in this area can be found in Foster (1976), Wyatt (1982), Fletcher et al. (1990), and Vernon et al. (1991).

This area is underlain by the crystalline rocks, composed of Piñon Flat Observatory granodiorite (Foster, 1976) of the middle Cretaceous age (90-100 my). This rock is unusually rich in biotite which can cause rapid weathering and make near-surface rocks decompose to grus.

The top 1 m of ground is nearly fully decomposed granodiorite. Below this depth, the weathered rock grades to highly competent grus at a depth of about 3 m. Evidence provided by drilling (Fletcher et al., 1990) suggests that, below 3 m to a depth of about 25 m, the material grades from grus to grus with cornerstones and then finally to jointed granodiorite.

However, this is a description for the average structure in the Piñon Flat. Wyatt (1982) reported that there are variations of thickness in the sedimentary layer, mostly consisting of non-jointed granodiorite. Such a variation is consistent with our inversion results, as some stations seem to have (almost) no low shear-modulus layer while others require a low shear-modulus layer in the upper 20-30 m (or more). But as we describe below, our approach can only recover an average shear-modulus structure, not really capable of recovering a thickness of sedimentary layer on the order of 1-10m.

Resolving such finer details would require other types of data such as higher-frequency seismic data. In this paper, we will focus on the analysis of colocated pressure and seismic data in the low frequency band from 0.005 Hz to 0.05 Hz and try to understand the limitations of our method.

2.2 Colocated Pressure and Seismic Sensors

Figure 2 shows the locations of seismic and pressure sensors within the Piñon Flat Observatory (the box in Figure 1). The numbers indicate station names; for example, 1 is station BPH01 (network code PY), 2 is BPH02, and so forth. There are thirteen stations from BPH01 to BPH13. Among 13 stations, pressure sensors are installed at nine of them (1, 3, 5, 6, 7, 9, 10, 11, and 12). The remaining four stations (2, 4, 8, and 13) are not equipped with pressure sensors and therefore not included in the analysis. For these nine colocated stations, we analyze their data from the entire year of 2017.

In addition to these 13 stations, there are PFO station in the Anza network (network code AZ), PFO station in the IDA-IRIS station (network code II) and another station TPFO. Because of the lack of availability of pressure data, these stations are not included in this study. TPFO actually has a pressure sensor (an infrasound sensor not a barometer) since November, 2018, but because we worked on data from the entire year of 2017 for other stations, the results for TPFO are not included in this study.

For the nine stations, station coordinates and their instruments are listed in Table 1. Pressure sensors are the same for all stations (Setra 278) but there are two different seismic sensors (STS-5A and Trillium 120). We remove instrument response by deconvolution, thus the differences in seismic instruments should not matter. But even before the removal of instrument response, seismic data are quite similar, as the two seismic sensors essentially have the same response as shown in Figure 3. It is clear that this difference between two types of seismic sensors cannot affect our results.

A red line is shown in Figure 2, which indicates location of the linear geophone array that Yong et al. (2016) installed in order to retrieve shallow seismic structure. The end points of this linear array are given in Table 1. It seems most natural to interpret that their results represent an average structure along this red line. When we compare our results, we use the results at the nearest station (BPH01) and also at three nearby stations BPH03, BPH05, and BPH09 (Figure 15).

A red circle in Figure 2 is the location of the borehole site in Fletcher et al. (1990). There were actually two boreholes but their locations overlap on the scale of this plot. We chose to use the location of deep borehole site in all figures of this paper (Table 1). Vs30 at this site was estimated from the S-wave speed profile in Fletcher et al. (1990). We discuss this point in more details when we summarize our results on Vs30.

3 METHOD

3.1 Basic Principle

We described our inversion procedure and its theoretical background in Paper 1 but we briefly go over the basic principles in this section. For this purpose, we use data from other stations in the EarthScope Transportable Array.

In this method we first create a pressure-seismic plot like the one in Figure 4 (left). This is for one of the TA stations (KMSC) in South Carolina. We computed pressure PSDs and seismic PSDs from every one-hour time interval in 2014 and plotted them. The horizontal axis is pressure PSD and the vertical axis is seismic PSD. Figure 4 is the case for 0.02 Hz. Blue circles are for vertical seismic data and red circles are for horizontal seismic data. For this pressure-seismic plot, we typically use ground velocity PSDs for seismic PSDs. Horizontal PSDs are the sum of PSDs from the north-south (NS) and the east-west (EW) components.

Figure 4 shows that when pressure PSDs are lower than about 1 (Pa^2/Hz), vertical PSDs are no longer highly coherent with pressure variations. Many points are at a relatively constant level and indicate that vertical amplitudes are not influenced by the local pressure changes. But when pressure PSDs become higher than about 1 (Pa^2/Hz), vertical seismic PSDs become proportional to pressure PSDs. This behavior suggests that vertical seismic amplitudes are now controlled by local, surface pressure changes. We refer to this transition pressure as the threshold pressure, which is about 1 (Pa^2/Hz), but its precise value seems to vary from station to station and is hard to determine precisely because of scatter in data (Tanimoto and Valovcin, 2016).

In our method, coherence between pressure and vertical seismic data plays an important role. Green points in Figure 4 represent one-hour time intervals when the coherence exceeded 0.8. Most green points are seen for pressure above 1 (Pa^2/Hz). This indicates that when vertical seismic PSDs and pressure PSDs become proportional above the threshold pressure, the coherence between them often become high.

Horizontal PSDs are typically larger than vertical PSDs by a factor of 100-1000 at 0.02 Hz because of tilt effects (Rodgers, 1968). In general, horizontal amplitudes do not have a threshold pressure as in Figure 4. Usually, horizontal amplitudes change with pressure for the entire range of pressure in the frequency range of our analysis (0.005-0.05 Hz). But highly coherent horizontal data (green points) are found in the same pressure range with vertical data (Figure 4, left).

Use of high-coherence data is an important step in our approach as it justifies us to drop some scattered data even for those above the threshold pressure (Figure 4, left). These scattered data points must have arisen from teleseismic surface waves, complexities in local atmospheric turbulence (Davidson,

2015; Garratt, 1992) and those in wind-pressure relations. Recent studies on wind and seismic data have shown (e.g., De Angelis and Bodin, 2012; Dybing et al., 2019; Johnson et al., 2019; Mohammadi et al., 2019; Naderyan et al., 2016) that wind effects on seismic motions can be quite complex. It is particularly so in a higher frequency range (> 1 Hz) but it is also true, to some extent, in the frequency range of this study (0.005-0.05 Hz). By selecting high-coherence time intervals for the analysis (green points in Figure 4), we definitely see much cleaner relations between pressure PSDs and seismic PSDs. We also focus our analysis on higher pressure ranges in which seismic signals are generally larger and the signal-to-noise ratios (S/N) become larger.

These high-coherence data also give us new perspectives from their phase information. If we examine phase difference between vertical displacement and pressure for each one-hour time interval, we find phase differences of about ± 180 degrees as in Figure 5 (bottom). Examples from three stations are shown in this figure. The concentrations of high-coherence data points near ± 180 degrees are clear in high pressure ranges. For these particular cases in Figure 5, we examined the pressure range that was higher than 10 Pa^2/Hz at 0.02 Hz.

The fact that pressure and vertical seismic data are coherent and their phase differences are ± 180 degrees means that we have a situation as illustrated in the top panel of Figure 5; as pressure changes on Earth's surface, ground surface responds elastically with the opposite sign, that is for positive pressure, ground surface is depressed downward (negative) and vice versa. This is in agreement with the seismometers observing the surface loading effects by pressure on the solid Earth.

An important feature of this phenomenon is that the frequency range is limited to a range from about 0.01 Hz to 0.05 Hz (Sorrells, 1971; Sorrells et al., 1971; Sorrells and Goforth, 1973). Sometimes we see good coherence at 0.005 Hz, and in such a case we include it in our analysis. But for higher frequencies above 0.05 Hz, coherence is almost always low. This high-frequency limit is undoubtedly imposed by the ocean-generated seismic noise (the primary microseism) which typically dominates in the frequency range between 0.05 Hz and 0.07 Hz (Haubrich and McCamy, 1969).

3.2 Procedure

3.2.1 Measurements

We formulate our inversion method based on the quantity

$$\eta(f) = \frac{S_z(f)}{S_p(f)} \tag{1}$$

where f is frequency (Hz), $S_z(f)$ is vertical seismic (velocity) PSD ($m^2/s^2/Hz$) and $S_p(f)$ is pressure PSD (Pa^2/Hz) for the same time interval. Unit for $\eta(f)$ is then $m^2/s^2/Pa^2$. In this study, we compute them for each one-hour long time series throughout the year of 2017.

In the frequency range of our inversion, that is from 0.005 Hz to 0.05 Hz, tilt effects are dominant in horizontal data (Rodgers, 1968). In this situation, we can show that a horizontal seismic PSD is related to a vertical seismic PSD by

$$S_H(f) = (\frac{g}{\omega c})^2 S_z(f) \tag{2}$$

where g is gravitational acceleration, ω is an angular frequency ($\omega = 2\pi f$), and c is the (wind-related) pressure-wave speed on Earth's surface. Typically, $c(f)$ is in the range $1 - 10$ (m/s) and is much smaller than sound speeds in the atmosphere (about 340 m/s). In this paper, we refer to $c(f)$ as the pressure-wave speed.

We adopt the source model by Sorrells (1971) as in our previous papers (Tanimoto and Wang, 2018, 2019). In this model, slow wind-related pressure changes sweep over a colocated station with speed $c(f)$. This means that its horizontal wavelength is c/f which varies with frequency. Accordingly, the depth extent of the solid Earth that influences $\eta(f)$ should also vary with frequency. In general, lower frequency data ($\eta(f)$) are influenced more from deeper structure.

Equation (2) indicates that the horizontal to vertical ratios of seismic PSDs (S_H/S_z) provide a way to estimate c(f). Also the fact that S_H is proportional to S_z means that S_H carries the same amount of information with S_z, once $c(f)$ is determined. Therefore, we formulate the inversion using only vertical data (S_z) for the underlying structure. We could also formulate the inversion using horizontal data but we chose vertical data because scatter in vertical data is typically smaller than scatter in horizontal data.

In practice, we measure both $S_z/S_p(= \eta)$ and S_H/S_p for frequencies between 0.005 Hz and 0.05 Hz. After estimating the pressure-wave speed $c(f)$ from their ratio, we do not use S_H/S_p for subsequent steps in the inversion.

Examples of measurements of $\eta(f)$ are shown in Figure 6, which is for station BPH11 for 0.015 Hz (Figure 6a and 6b) and 0.035 Hz (Figure 6c and 6d). Measurements are actually made in Figures 6b and 6d. Figures 6a and 6c show pressure-seismic plots from which we judge the quality of colocated data. In Figure 6a, the top panel is the pressure-seismic plot for vertical data and the bottom is the pressure-seismic plot for horizontal data. Green points indicate high-coherence time intervals when the coherence was higher than 0.7 for this case.

In order to determine $S_z/S_p(\eta)$ and S_H/S_p, we could fit lines by the least-squares in pressure-seismic plots and estimate them from the gradients of the best-fit lines. But instead we use a different approach; we make plots for $S_z/S_p(\eta)$ and S_H/S_p plotted against S_p as in Figures 6b and 6d. The ratios should approach constant values toward a higher pressure range. We select high coherence points (green) from a high pressure range and estimate these ratios.

In Figures 6b and 6d, we indicate the selected range of data by boxes. After the selection, we

simply compute the average and uncertainties for these points. There is some ambiguity in selecting the bounds of these boxes but as green points approach constant values at high pressure, their average values are not affected very much for a different selection of data (Tanimoto and Wang, 2019).

A question may arise as to why we only focus on a very high pressure range and do not use high-coherence points from lower pressures. We chose this approach mainly because scatter of green points (vertical spread of green points in Figures 6b and 6d) becomes larger for lower pressures. Also, in general, we believe measurements of $\eta(f)$ become more reliable at higher pressure as ground deformation caused by surface pressure becomes dominant and eclipses contributions from other noise sources. Coherence is a useful guide for data selection but in practice we have to set its cut-off level at about 0.6-0.8. It cannot eliminate effects from other noise sources entirely. We believe that focusing on data from a very high pressure range is a much more prudent approach.

We apply the same procedure to the range between 0.005 Hz and 0.05 Hz at an interval of 0.005 Hz and measure the ratios $S_z/S_p(=\eta)$ and S_H/S_p. Then we determine the pressure-wave speed $c(f)$ from their ratios. We also compute $\overline{\mu}$ for each frequency by using a formula $\overline{\mu}(f) = (c/2)\sqrt{S_p/S_z}$. This is based on a relation when the solid Earth is a homogeneous half-space: $\eta(f) \equiv S_z/S_p = c^2/(4\overline{\mu}^2)$ (Sorrells, 1971; Tanimoto and Wang, 2018). Using two elastic constants, λ and μ, in the homogeneous half-space, this parameter is defined by $\overline{\mu} = \mu(\lambda+\mu)/(\lambda+2\mu)$. Here, μ is the shear modulus and λ is the Lame's constant if the solid Earth were a homogeneous half-space.

In general, we find that $\overline{\mu}(f)$ varies with frequency as the medium beneath a colocated station is not a homogeneous half-space. Its variation with frequency is a good indicator for a layered structure. We also use this quantity to construct a starting model for the inversion.

We tabulate all measured values for each station in Tables 3-11.

3.2.2 Starting model

We use $\overline{\mu}(f)$ to derive a starting model for the iterative, nonlinear inversion that follows. Here, we briefly summarize the main steps, although more details can be found in Tanimoto and Wang (2019).

Before adopting the procedure we describe below, we initially attempted to use a homogeneous half-space solution at 0.02 Hz for the starting model. We chose 0.02 Hz because pressure and seismic data generally show the highest coherence and the best signal-to-noise ratio for $\eta(f)$ at this frequency. The iterative nonlinear inversion with this starting model worked for a number of stations but it did not converge for some stations. In order to improve this situation, we decided to incorporate more information by using $\eta(f)$ from the entire frequency range. We thus use all $\overline{\mu}(f)$, typically between 0.01 Hz and 0.04 Hz (Tables 3-11), for each station.

In this approach, in addition to $\overline{\mu}(f)$, we also use a standard shallow-structure model, the model

BJ97gr760, by Boore (2016). This model was constructed from a collection of many shallow-structure models and provides density (ρ), P-wave speed (α), and S-wave speed (β) as a function of depth at very shallow depths. For each measurement of $\overline{\mu}(f)$, we search this model in depth and find the best match for each $\overline{\mu}(f)$. We thus get a set of parameters ρ_i, α_i and β_i that has the same value of $\overline{\mu}(f)$ (Here we introduced a subscript i to specify frequency).

We performed many computations of depth sensitivity kernels of $\eta(f)$ for density, shear modulus and bulk modulus previously (Tanimoto and Wang, 2019). Results indicated that the shear-modulus kernel has the maximum value in comparison to other kernels. We also found that its peak depth is at about $h = 0.15c(f)/f$ (m), where the unit for $c(f)$ is m/s and that for f is in Hz. This peak depth should change with different density and seismic parameters but their variations were surprisingly small. In other words, the most sensitive depth for $\eta(f)$ is almost always given (approximately) by this depth h. We refer to this depth as h_i (i=1,2,...,n), where n is the number of frequencies used for inversion. We thus obtain a set of values (h_i, ρ_i, α_i, β_i) and align them in depth. Let us define h_1 be the shallowest depth (knot) and h_n the deepest.

We simply interpolate these values linearly and determine density, P-wave speed and S-wave speed between h_i and h_{i+1} (i=1,2,...,n-1). From the surface to the shallowest knot (h_1) we assume a homogeneous structure with $(\rho_1, \alpha_1, \beta_1)$. Similarly, for the deeper region below the deepest knot (h_n), we assume a homogeneous half-space with ($\rho_n, \alpha_n, \beta_n$).

This simple procedure has given us a starting model that converged in most cases. It is worth noting that we use colocated pressure and seismic data to construct this starting model in order to invert the same dataset. Therefore, the starting models are different for each colocated station.

We have not examined the uniqueness of this inversion scheme, however. The fact that the iterative inversion from a homogeneous half-space model did not converge for some cases suggests that there may be local minimums for the objective function we chose (section 3.2.4). We intend to improve our understanding on these questions but in this paper, we simply present an inversion procedure to obtain a solution that matches measurements of $\eta(f)$.

3.2.3 Coherence threshold

In order to apply our measurement procedure as described with Figure 6, it is necessary to have a number of high-coherence (green) points. We have found, however, that this number varies from station to station. We chose a threshold coherence value of 0.7 in Figure 6, but for some other stations we had to use a different threshold value.

If we lower the threshold value, we can have a larger number of high-coherence points. But there is a penalty for this change that appears in the scatter of points. Therefore, for each station, we tried a

few different coherence threshold values and tried to decide an optimal value. For example, the optimal coherence threshold for BPH11 was 0.7 (Figure 6).

Figure 7 shows the pressure-seismic plots for all nine stations at 0.02 Hz. We are showing the plots for 0.02 Hz because coherence typically reaches its maximum at 0.02 Hz for a given station (within the frequency range 0.005-0.05 Hz).

The plots in Figure 7 are based on the coherence threshold of 0.6. We can see a fairly large number of green (high-coherence) points for BPH03, BPH05, BPH07, BPH09, BPH10, and BPH11 but smaller numbers of green points for BPH01, BPH06 and BPH12. We judged that the number of points for BPH01, BPH06 and BPH12 are too few to make an estimate for $\eta(f)$. Therefore, we reduced the lower threshold value to 0.5 for these stations. The results of this paper are based on the coherence threshold value of 0.6 for BPH07, BPH09, and BPH10, and 0.7 for BPH03, BPH05, and BPH11. The measured values of $\eta_o(f)$ are tabulated in nine tables from Tables 3 to Table 11.

In general, there is a correlation between the stiff structure beneath a station (typically hard-rock sites) and a smaller number of high-coherence points. This is because when the underlying medium is stiff, seismic deformation caused by surface pressure changes becomes generally small, leading to low signal-to-noise ratios (S/N) in seismic data. Coherence becomes naturally low for such low S/N data.

3.2.4 Inversion for structure

In Paper 1, we discussed an approach for theoretical computation of $\eta(f)$ for a vertically heterogeneous structure. We use the source representation by Sorrells (1971) which specifies a surface boundary condition for pressure. Combined with three other boundary conditions, the vanishing of shear stress at the surface and two radiation conditions in the lowermost half-space, we can integrate the P-SV system of equations (e.g.,Takeuchi and Saito, 1972). More details can be found in Paper 1.

We also noted that the compound matrix formulation (e.g., Takeuchi and Saito, 1972) can be used for surface observation of pressure and seismic data. Its extension to a perturbation problem, that is to compute a change in η when structural parameters are perturbed (perturbations of density and two elastic constants or density and P-wave and S-wave speeds), can be performed by numerical differentiations. This is the critical step for formulating the inversion. We can write this relation by an integral

$$\frac{\delta\eta}{\eta} = \int_{-\infty}^{H} (K_\rho \frac{\delta\rho}{\rho} + K_\kappa \frac{\delta\kappa}{\kappa} + K_\mu \frac{\delta\mu}{\mu}) dz, \tag{3}$$

where K_ρ is the density kernel, K_κ is the bulk-modulus kernel and K_μ is the shear-modulus kernel, and z is the vertical coordinate. These kernels are functions of frequency as well as density and seismic

velocities. We take the z-axis upwardly positive; the surface is at $z = H$. A stack of layers is assumed to exist between $z = 0$ and $z = H$ and the lowermost homogeneous half-space occupies the region $z < 0$. We call these kernels as depth sensitivity kernels.

For our problem, we demonstrated numerically that the density kernel is very small and may be dropped from the inversion when we take two elastic constants as other independent parameters (Paper 1). In such a case, we can write

$$\frac{\delta\eta}{\eta} = \int_{-\infty}^{H} (K_\kappa \frac{\delta\kappa}{\kappa} + K_\mu \frac{\delta\mu}{\mu}) dz. \tag{4}$$

This formula is the basis for an iterative, nonlinear inversion procedure; for an assumed (1D) starting model, we compute the theoretical values η_t, the bulk-modulus kernel $K_\kappa(z)$ and the shear-modulus kernel $K_\mu(z)$ for each frequency. If we denote the observed $\eta(f)$ by $\eta_o(f)$, we can replace the lefthand side of this equation by η_o and η_t and write the inversion formula as

$$\frac{\eta_o(f) - \eta_t(f)}{\eta_t(f)} = \int_{-\infty}^{H} (K_\kappa \frac{\delta\kappa}{\kappa} + K_\mu \frac{\delta\mu}{\mu}) dz. \tag{5}$$

For a given structure, there is usually a discrepancy (misfit) between η_t and η_o which leads to a non-zero value (misfit) on the left-hand side. Discretizing the integration on the right-hand side into **n** layers and combining equations from different frequencies, the (matrix) equation can be set up as

$$\mathbf{A}\mathbf{x} = \mathbf{d} \tag{6}$$

where the righthand side is the data vector defined by

$$\mathbf{d} = [\Delta\eta_1, \Delta\eta_2, ..., \Delta\eta_m]^T \tag{7}$$

where T means the transpose of a matrix (vector) and $\Delta\eta_i = (\eta_o(f_i) - \eta_t(f_i))/\eta_t(f_i)$. Here we have a matrix equation because we combined $\Delta\eta_i$ from different frequencies ($i = 1, 2, ..., m$) and m is the number of different frequencies we invert.

We define the solution vector $\mathbf{x}$ by

$$\mathbf{x} = [(\frac{\delta\kappa}{\kappa})_1, (\frac{\delta\kappa}{\kappa})_2, ..., (\frac{\delta\kappa}{\kappa})_n, (\frac{\delta\mu}{\mu})_1, (\frac{\delta\mu}{\mu})_2, ..., (\frac{\delta\mu}{\mu})_n]^T \tag{8}$$

where the subscripts are the layer numbers. Because each layer has two elastic constants to be solved for, we have $2n$ elements in this vector.

The matrix $\mathbf{A}$ is defined by

$$\mathbf{A} = \begin{pmatrix} K_\kappa^{11} & K_\kappa^{12} & \dots & K_\kappa^{1n} & K_\mu^{11} & K_\mu^{12} & \dots & K_\mu^{1n} \\ K_\kappa^{21} & K_\kappa^{22} & \dots & K_\kappa^{2n} & K_\mu^{21} & K_\mu^{22} & \dots & K_\mu^{2n} \\ \vdots & \vdots & \vdots & \vdots & \vdots & \vdots & \vdots & \vdots \\ K_\kappa^{m1} & K_\kappa^{m2} & \dots & K_\kappa^{mn} & K_\mu^{m1} & K_\mu^{m2} & \dots & K_\mu^{mn} \end{pmatrix} \Delta z \tag{9}$$

where the size of this matrix is $m \times 2n$. In this study, we used a stack of homogeneous layers with the same thickness of 0.5 m, thus $\Delta z = 0.5$ m.

We solve this matrix equation by the damped least squares (e.g., Aki and Richards, 2002). With a damping constant $\epsilon^{\mathbf{2}}$, a solution can be written by

$$\bar{\mathbf{x}} = (\mathbf{A^T A} + \epsilon^{\mathbf{2}}\mathbf{I})^{-\mathbf{1}}\mathbf{A^T d} \equiv \mathbf{L d} \tag{10}$$

where we defined the operator $\mathbf{L}$. We then update the structure by this solution $\bar{\mathbf{x}}$ and go on to the next step of iteration.

The starting model is constructed by following the procedure in Paper 1. We iterated this nonlinear inversion process, typically 10 times. But we found in all nine cases that the solution for the second iteration step is sufficiently close to the final model. For all cases in this paper, the solution for the second iteration is regarded as the final model.

We estimate the uncertainties for $\bar{\mathbf{x}}$ by using the relation between the covariance matrix for model parameters $\bar{\mathbf{x}}$ ($\mathbf{C}_{\bar{\mathbf{x}}\bar{\mathbf{x}}}$) and the data covariance matrix for data $\mathbf{d}$ ($\mathbf{C_{dd}}$) (e.g., Aki and Richards, 2002):

$$\mathbf{C}_{\bar{\mathbf{x}}\bar{\mathbf{x}}} = \mathbf{L C_{dd} L^T} \tag{11}$$

Following the convention for this type of least-squares solution, we assume that the data covariance matrix is a diagonal matrix (each measurement is independent) and the diagonal elements of $\mathbf{C}_{\bar{\mathbf{x}}\bar{\mathbf{x}}}$ can be used for the uncertainty estimates of $\bar{\mathbf{x}}$. These uncertainties are for shear-modulus and bulk-modulus parameters and they are propagated to S-wave speed model with empirical relations for density (Boore, 2016) in order to determine Vs30. For each iteration step, we obtain these uncertainties but we have found that they do not change very much from iteration to iteration. This is probably related to the fact that the major variance reduction occurs only in the first iteration. The uncertainties for Vs30 (Table 2) were estimated through these procedures.

3.2.5 Example of Inversion : BPH11

Figure 8 summarizes an example of our inversion procedure for station BPH11. We measured $\eta_o(f)$ by using a procedure in Figure 6 for frequencies between 0.01 Hz and 0.04Hz at an interval of 0.005 Hz. These measured values are shown in Figure 8b with uncertainties. Each error bar indicates a range for one standard deviation ($\pm 1\sigma$). Theoretical $\eta(f)$ values for the starting model, the first iteration model and the second iteration model are shown by the blue, green and red lines in Figure 8b.

Figure 8a shows the reduction of variances (misfits) at each iteration step. The variance was computed by

$$\mathrm{VAR} = \sum_{i=1}^{N} \{\eta_o(f_i) - \eta_t(f_i)\}^2 \tag{12}$$

where i is an index for frequency, in this case from 0.01 Hz to 0.04 Hz at an interval of 0.005 Hz, thus $N = 7$. The values plotted in Figure 8a are normalized by the variance for the starting model. The main point of this figure is that the largest variance reduction occurred in the first iteration.

The shear-modulus and bulk-modulus structures are shown in Figure 8c for the starting, the first iteration and the second iteration models. As we mentioned above, we regard the solution at the second iteration as the final model in this paper.

The inverted structures in Figure 8c show that the data require a low shear-modulus zone approximately in the upper 30 m. On the other hand, the bulk-modulus structure hardly changed from the starting model.

Figure 8d shows density, P-wave and S-wave speed structures for the final model. We use the density structure in the starting model in order to convert the bulk-modulus and shear-modulus results to P-wave and S-wave speed models.

After getting the final S-wave speed model (Figure 8d), we estimate Vs30 from

$$\frac{30}{Vs30} = \int_{H-30}^{H} \frac{dz}{\beta(z)} \tag{13}$$

where the integration on the righthand side is for the upper 30m from the surface ($z = H$). For station BPH11, we got $Vs30 = 603$ (m/s).

The reason that we only saw small changes for the bulk-modulus structure may be understood from the kernels in (4) and Figure 9. Figure 9 shows the shear-modulus kernels at top and the bulk-modulus kernels at bottom. They are from the first iteration step when the major variance reduction occurred. Shape of these kernels can change for each iteration step but in practice we have found very small differences. Note that the two panels in Figure 9 are plotted on the same scale. Clearly, except for the upper 10-20 m, the bulk-modulus kernels are much smaller than the shear-modulus kernels. This feature means that the data may have some sensitivity to the bulk-modulus structure in the top 20 m but are mostly sensitive to the shear-modulus structure in the upper 50-100m.

In Table 2, we show Vs30 for our starting models within parentheses. Because our starting models are constructed from the entire frequency range of $\overline{\mu}(f)$, these values are quite close to our final estimates of Vs30. They are typically within 5 percent of our final estimates. But they do not fit our measured $\eta(f)$ in an optimal sense.

4 INVERSION RESULTS AND THE MAIN CHARACTERISTICS

We applied the same inversion procedure to all nine colocated stations in the Piñon Flat Observatory. For every station, we examined the effects of changing the frequency range of data, specifically on

how they incluence the derived structures and the estimates of Vs30. The results are summarized in Table 2, Figures 10-12 and also in Figures S1-S9.

Table 2 lists the results for all stations. We selected a representative case for each station (marked by X) for which we show the inversion processes in Figure 10 (BPH01, 03, 05), Figure 11 ((BPH06, 07, 09) and Figure 12 (BPH10, 11, 12). Later, we compare the structures for BPH01, BPH03, BPH05 and BPH09 against the models reported in Yong et al. (2016). All other cases are shown in the Appendix from Figure S1 (BPH01) to Figure S9 (BPH12).

In this section, we point out three main characteristics in these results. The first point is that a choice of frequency range for the inversion does not affect our estimate of Vs30. Here, we mean by the word 'choice', either the inclusion of 0.005 Hz data in the inversion or the inclusion of data above 0.04 Hz. We found that exclusion of data below 0.01 Hz and above 0.04 Hz can only change Vs30 by a few percent.

The second point is that our method can only derive averaged, smooth structures in the upper 50-100 m, as opposed to distinct layers derived by others such as the one by Yong et al. (2016). In order to clarify this point, we compute the depth resolution kernels for each case of inversion and show that the kernels have broad peaks in the upper 50 m with relatively small variations from station to station. We claim, however, that this lack of resolution for fine structures does not affect our estimate of Vs30 very much because Vs30 is an averaged quantity from the uppermost 30 m.

The third point is on the large spatial variations in Vs30. A summary map of Vs30 suggest that the result at BPH06 is anomalous because Vs30 is much larger than nearby stations. But we point out that the absolute observed values of η_o can be measured reliably and are sensitive to the stiffness of the medium. Small observed values of η_o support that the medium beneath BPH06 is quite stiff, resulting in a high value of Vs30. It also suggests that a sedimentary layer is thin, even if it existed.

4.1 Frequency range

We discuss the effects from data at 0.005 Hz and those from above 0.04 Hz separately. In either case, we will show that exclusion of these data from the inversion does not seem to affect our estimates for Vs30 very much.

4.1.1 Influence of data at 0.005 Hz

We found the coherence between pressure and seismic data is generally high between 0.01 Hz and 0.05 Hz but occasionally we also found high coherence at 0.005 Hz. For such stations, we included the measurement at 0.005 Hz in the inversion.

The main effects of including data (η_o) at 0.005 Hz seem to arise in the derived structure below

30 m in depth. The case for BPH01 (Figure S1) is a clear example; the frequency ranges of three inversions for this station were 0.005 Hz-0.030 Hz (Figure S1a), 0.005 Hz-0.035 Hz (Figure S1b), and 0.010 Hz - 0.035 Hz (Figure S1c). A feature that is common in Figures S1a and S1b but is lacking in Figure S1c should be related to the effects from data at 0.005 Hz. The shear-modulus structures (in the middle panels) show that a gradual increase of shear modulus and bulk modulus is found from about 20m to 70 m in Figures S1a and S1b but not in Figure S1c. In Figure S1c, the hear-modulus structure and the bulk-modulus structure are basically constant from the depth about 30 m to deeper regions. Similar effects on deeper structures from the inclusion of 0.005 Hz data can also be found in Figure S7 (BPH10) and Figure S8 (BPH11).

In these cases, an inclusion of data at 0.005 Hz modifies shear-modulus structures below a depth about 30 m. Clearly, such a change cannot affect our estimates of Vs30 (Table 2).

4.1.2 Influence of data above 0.040 Hz

While we measure coherence from 0.005 Hz to 0.05 Hz for all cases, coherence shows a decreasing trend above 0.04 Hz at some stations. The uncertainties that are estimated for these data above 0.04 Hz also tend to become large. For example, Figures S5c (BPH07) and S8c (BPH11) show the results that included the measurements of η_o at 0.045 Hz. Both cases show large error bars at 0.045 Hz that are specifically larger than error bars at frequencies below 0.04 Hz. Also, the mean values at 0.045 Hz seem to be systematically shifted in comparison to the trend in data below 0.04 Hz.

We suspect that there could be contamination effects from the ocean-generated microseism (the primary microseism) for frequencies above 0.04 Hz. Even though the primary microseism is typically confined to the frequency range above 0.05 Hz (0.05-0.07 Hz), some signals may be generated below 0.05 Hz in its energetic seasons. Furthermore, more unusual ocean-generated seismic noise, such as the 26-sec (0.038 Hz) signals (Shapiro et al., 2006) may also destroy coherence between pressure and seismic data. In such a case, we may have to drop data even at 0.04 Hz but such signals seem to be rare. In this paper, we excluded data above 0.04 Hz in the final models.

If the data above 0.04 Hz were included, as for BPH07 (Figure S5) and BPH11 (Figure S8), there are some effects on our estimates for Vs30, as these high-frequency data should modify shallow structure. But the difference in estimated Vs30 for BPH07 is about 1 percent and the difference for BPH11 is about 2 percent (Table 2). Therefore, the loss of information from the exclusion of data above 0.04 Hz does not seem to be important for estimating Vs30.

4.2 Depth resolution

For each case of inversion, we obtained the depth resolution kernels. The kernels for the selected cases in Figures 10-12 are shown in Figure 13. Other cases in the Appendix are quite similar.

Strictly speaking, since our approach is a nonlinear iterative inversion, the definition of the depth resolution kernel is not straightforward. But because most variance reductions occur in the first step of inversion (for all cases), we believe we are justified to use the case of first iteration to understand the depth resolving power of our data.

In our notation, we can compute the resolution matrix (e.g., Aki and Richards, 2002) by

$$\mathbf{R} = (\mathbf{A^T A} + \epsilon^2 \mathbf{I})^{-1} \mathbf{A^T A}. \tag{14}$$

which contain depth resolution information for shear-modulus and bulk-modulus structures at various depths. We just need to select the relevant elements to the depth resolution kernels.

Figure 13 shows the depth resolution kernels of shear modulus for all nine cases. They show the cases for the target depth of 20, 40, 60, and 80 m, plotted in different colors.

For the target depth of 20 m, the kernels typically peak near 20 m with a half-width (the width of a kernel at half the peak amplitude) varying in depth from about 10 m to 60 m. There are some variations from station to station but the differences appear small. For example, the kernels for BPH05 show the broadest peaks, whose deepest parts reaching beyond 100m. On the other hand, the kernels for BPH01 and BPH07 are confined to shallow depths. The kernels seem to disappear almost entirely at 80m.

These differences between different stations are small, however, and shape of these shear-modulus kernels indicates that the derived shear modulus at depth 20 m represents an averaged value approximately from the upper 50 m. The peak depth of the kernel basically matches with the target depth of 20 m.

For deeper target depths at 40m, 60m and 80m, however, the peak of the kernels deviate from the target depths. These deviations seem to increase for deeper target depths and the widths of kernels also increase for deeper target depths.

In summary, Figure 13 shows that the depth resolving power of our dataset, that is $\eta(f)$ from about 0.005 Hz to 0.04 Hz, is rather limited. But it also shows that an average shear-modulus structure in the upper 50 m is recoverable by this inversion method. Furthermore, since our structures are fairly smooth throughout the upper 50 m, our estimates for Vs30 are quite stable as the Vs30 estimates in Table 2 show.

4.3 Absolute values of η

The plots from Figures 10 to 12 (and Figures S1 to S9) may tend to emphasize the variations of $\eta(f)$ as a function of frequency. But the absolute values of the data are also important.

Take, for example, the cases of BPH05 and BPH06. In Figures 10 (right) and Figure S3, the ratios of $S_z/S_p(\equiv \eta_o)$ vary from about 1×10^{-18} to 3×10^{-18} in MKS units. On the other hand, η_o in Figures 11 (left) and Figure S4 are about 2×10^{-19} in MKS units, making them smaller than those for BPH05 by a factor of about 5-10.

Smaller $\eta(\equiv S_z/S_p)$ means, for a given pressure strength (S_p), seismic PSDs (S_z) are smaller, suggesting a stiffer underlying medium that is difficult to deform. These differences are also (eventually) reflected on the estimates of Vs30 which are about 979-981 (m/s) for BPH05 and 1489-1549 (m/s) for BPH06. Vs30 for BPH06 may appear anomalously high in comparison to nearby stations (Figure 15) but it is consistent with the observed amplitude values of η_o.

Clearly, not only the frequency variations of $\eta(f)$ but their absolute values carry important information for the elastic property of the solid Earth.

5 COMPARISON TO USGS MODEL AND VS30 MAP

5.1 Comparison of structures

The closest station to the study area by Yong et al. (2016) is BPH01 but three other stations, BPH03, BPH05 and BPH09 are also close. The location of this USGS study is indicated by the red line in Figure 2 (and Figure 15). Yong et al. (2016) also performed the H/V type analysis at PFO station of the Anza Network (station code AZ) but their main results are mostly from the linear geophone array along this red line.

Their estimates for Vs30 was spread over a range from 685 to 840 (m/s) because they used multiple methods for the estimates and the results varied within this range. Among their structures based on different types of data, we chose models based on the Rayleigh-wave analysis (MASW) and the Love-wave analysis (MALW) from their geophone array data. In Figure 14, we compare our models for BPH01 (red), BPH03 (green), BPH05 (magenta), and BPH09 (blue) against their three models; they are a Rayleigh-wave model with Poisson's ratio (PR) of 0.2 (thick black), a Rayleigh-wave model with Poisson's ratio 0.3 (dashed black), and a Love-wave model with Poisson's ratio 0.3 (dotted black). For this comparison, we converted their results to shear-modulus structures.

Figure 14 shows that our structures are much smoother than their models. Since Yong et al. (2016) used relatively high frequency data above 1 Hz, their approach was able to derive more detailed structures within the top 30 m. In constrast, we observe a low-frequency elastic response of the solid Earth

(0.005-0.04 Hz) caused by surface pressure loading effects. This elastic response can be modeled as quasi-static deformation of the Earth (e.g., Sorrells, 1971). Such a phenomenon can only give us an averaged shear-modulus structure from shallow depths.

Despite this lack of fine structures in our model, our estimates for Vs30 and those by Yong et al. (2016) are close. For example, our estimates for Vs30 at BPH01 is 738 (m/s) while Yong et al.'s estimates along the red line vary 673, 744 and 779 (m/s). In their summary they list their Vs30 as 685-840 (m/s) because they also used other data. These numbers suggest that while our method is limited to recovering a smooth structure, it can recover a depth-averaged quantity like Vs30.

5.2 Comparison with Active Source Results

Figure 15 summarizes our estimates for Vs30. We represent Vs30 for each station by the selected cases in Table 2 (marked by X). These are the same with cases in Figures 10-12.

We also estimated Vs30 at the borehole site (the red circle in Figure 15), using the S-wave speed profile in Fletcher et al. (1990). Figure 16 is our reconstruction of Figure 4 in Fletcher et al. (1990) and shows their S-wave speed model in the uppermost 50 m. S-wave speeds are given at an interval of 2.5 m from the surface. We simply applied the equation (13) to this structure and obtained $Vs30 = 702$ m/s.. But this interval of 2.5 m is coarse for the purpose of estimating Vs30. In order to understand a possible range of Vs30, we perturbed the model in various ways. For example, if we shifted S-wave speeds by one grid (2.5 m), Vs30 estimate changed between about 600 and 800 (m/s). In general, small perturbations can change this Vs30 estimate by about 100 (m/s) quite easily. In Table 2, we assign an uncertainty of 100 based on these perturbations to the model, but it is clear this uncertainty estimate has no statistical basis. The real uncertainty can be larger than 100.

Figure 15 also shows that Vs30 contains fairly large spatial variations. If two locations are separated by about 100m, Vs30 can be quite different. We believe that these variations are mostly true and may be explained by the variations in the thickness of shallow sedimentary layer. As we discussed in section 2, weathering effects are important in this area. Considering the slopes on Earth's surface in the area (Figure 1), thickness of the sedimentary layer can change in the horizontal directions by lateral transport of sedimentary materials (grus).

6 CONCLUSIONS

We applied our method of inverting colocated pressure and seismic data to nine colocated stations in the Piñon Flat Observatory and obtained shallow elasticity structures beneath each station. We analyzed one-year long data for each station from the entire year of 2017.

The results showed that our method was capable of recovering shear-modulus structure approximately in the upper 50 m. The Vs30 value estimated for the station BPH01 was close to an independent estimate by Yong et al. (2016). Our estimates of Vs30 at nearby stations BPH03, BPH05, and BPH09 were also close. Our estimate of Vs30 at the borehole site (Fletcher et al., 1990) also generally agreed with Vs30 estimate at BPH09 and the USGS estimates, considering the uncertainties associated with the estimates.

Our method can only derive a smooth, depth-averaged structure because it analyzes slow deformation of the Earth by surface pressure changes in a low frequency band (0.005-0.05 Hz). This slow deformation is controlled by an average elastic property of the medium mostly in the upper 50 m of the Earth. The derived structures lack fine layerings and also sharp discontinuities. However, we can still get close estimates for Vs30 because Vs30 is an integrated property from the uppermost 30 m of the Earth.

ACKNOWLEDGMENTS

We thank Victor Tsai, Ralph Archuleta, and an anonymous reviewer for making suggestions on the manuscript. We also thank Frank Vernon and Joe Fletcher for providing us detailed information on the borehole data at PFO. All seismic and pressure data used in this paper (UC San Diego, 2014, network PY) were obtained from the IRIS DMC (the Data Management Center of the Incorporated Research Institutions for Seismology). We are grateful for their efficient service. This study was partially supported by grants from the National Science Foundation (NSF EAR 1547523) and the US Geological Survey (USGS G19AS00033). It was also supported by the Southern California Earthquake Center (Contribution No. 10026). SCEC is funded by NSF Cooperative Agreement EAR-1600087 & USGS Cooperative Agreement G17AC00047. The data in this study and associated inversion files can be found from http://doi.org/10.105281/zenodo.3600630 .

REFERENCES

Aki, K. and P. G. Richards (2002). *Quantitative Seismology: Theory and Methods*, 2nd edition, Sausalito: University Science Books.

Allen, T. I. and D. J. Wald(2009). On the use of high-resolution topographic data as a proxy for seismic site condition (Vs30), *Bull. seism. Soc. Am/*, *99(2A)*, 935-943, https://doi.org/10.1785/0120080255

Boore, D. M. (2016), Determining generic velocity and density models for crustal amplification calculations, with an update of the boore and joyner (1997) generic site amplification for Graphic Site Amplification, *Bulletin of the Seismological Society of America*, *106*(1), 313, doi: 10.1785/0120150229.

Boore, D. M., Joyner, W. B. and Fumal T. E. (1997), Equations for estimating horizontal spectra and peak acceleration from Western North American Earthquakes: a summary of recent work *Seismo. Res., Lett.*, *68*, 128-153.

Bozorgnia Y., Abrahamson N.A., Al Atik L., Ancheta T.D., Atkinson G.M., Baker J., Baltay A., Boore D.M, Campbell K.W., Chiou B.-S.J., Darragh R.B., Day S., Donahue J., Graves R.W., Gregor N., Hanks T., IdrissI.M., Kamai R., Kishida T., Kottke A., Mahin S.A., Rezaeian S., Rowshandel B., Seyhan E., Shahi S., Shantz T., Silva W.J., Spudich P., Stewart J.P., Watson-Lamprey J., Wooddell K.E., Youngs R.R. (2014), NGA-West2 research project, *Earthq. Spectra* , *30*(3): 973987.

Brocher, T. M. (2005), Empirical relations between elastic wavespeeds and density in the earth's crust, *Bulletin of the Seismological Society of America*, *95*(6), 2081, doi: 10.1785/0120050077.

Davidson, P. A. (2015). *Turbulence*, second edition, Oxford University Press, Oxford, UK.

De Angelis, S. and P. Bodin (2012). Watching the wind: Seismic data contamination at long periods due to atmospheric pressure-field-induced tilting. *Bull. seism Soc. Am.*, **102(3)**, 1255-1265, https://doi.org/10.1785/012110186

Dybing, S., Ringler, A., Wilson, D., and Anthony, R. (2019). Characteristic and spatial variability of wind noise on near-surface broadband seismometers, *Bull. seism Soc. Am.*, **109(3)**, 1082-1098, https://doi.org/10.1785/0121180227

Fletcher, J. B., T. Fumal, H.-P. Liu, and L. C. Carroll (1990). Near-surface velocities and attenuation at two boreholes near Anza, California, from logging data. *Bull. Seism. Soc. Am.*, **80**, No. 4, 807-831.

Foster, J. (1976). Geology, in *Deep Canyon, a Desert Wilderness for Science*, edited by I. P. Ting and W. Jennings, p90-91, University of California, Riverside.

Garratt, J. R. (1992). *The Atmospheric Boundary Layer*, Cambridge University Press, Cambridge, UK.

Goulet, C., Y. Bozorgnia, N. Kuehn, L. Atik, R. Youngs, R. Graves, G. Atkinson (2017). NGA-East ground-motion models for the U. S. Geological Survey National Seismic Hazard Maps, *PEER Report No. 2017/03*, Pacific Earthquake Engineering Research Center, University of California, Berkeley, CA.

Haubrich, R. A. and K. McCamy (1969). Microseisms: Coastal and pelagic sources, *Rev. Geophys.*, **7**, 539-571.

Johnson, C. W., Meng, H., Vernon, F. and Ben-Zion, Y. (2019) Characteristics of Ground Motion Generated by Wind Interaction with trees, structures, and other surface obstacles, *J. Geophys. Res.: Solid Earth*, **124**. 8519-8539, https://doi.org/10.1029/2018JB017151.

Mohammadi, M., C. J. Hickey, R. Raspet, and V. Naderyan (2019). Wind-induced ground motion: Dynamic model and nonuniform structure for ground *J. Geophys. Res.: Solid Earth*, **124**. https://doi.org/10.1029/2019JB017562

Naderyan, V., Hickey, C. J. and R. Raspet (2016). Wind-induced ground motion, *J. Geophys. Res.: Solid Earth*, **121**, 917-930, https://doi.org/10.1029/2015JB012478

Park, S., and M. Ishii (2018). Near-surface compressional and shear wave speeds constrained by body-wave polarization analysis, *Geophysical Journal International*, *213*(3), 1559–1571, doi: 10.1093/gji/ggy072.

Rodgers, P. (1968). The response of the horizontal pendulum seismometer to Rayleigh and Love waves, tilt, and free oscillations of the Earth *Bull. seism Soc. Am.*, **58**, 1385-1406.

Shapiro, N. M., M. Ritzwoller, and G. Bensen (2006). Source location of the 26 sec microseism from cross-correlation of ambient seismic noise *Geophys. Res. Lett.*, **33**, L18310 doi:10.1002/2006GL027010

Shearer, P. M., and J. A. Orcutt (1987), Surface and near-surface effects on seismic waves theory and borehole seismometer results, *Bulletin of the Seismological Society of America*, *77*(4), 1168.

Sorrells, G. (1971). A preliminary investigation into the relationship between long-period seismic noise and local fluctuations in the atmospheric pressure field *Geophys. J. R. Astr. Soc.*, **26**, 71-82.

Sorrells, G., J. A. MacDonald, Z. Der, and E. Herrin (1971). Earth motion caused by local atmospheric pressure changes, *Geophys. J. R. Astr. Soc.*, **26**, 83-98.

Sorrells, G., and T. Goforth (1973). Low-frequency earth motion generated by slowly propagating partially organized pressure fields, *Bull. Seism. Soc. Am.*, **63**, 1583-1601.

Takeuchi, H. and M. Saito (1972). Seismic surface waves, *Methods in Computational Physics*, Vol. 11, edited by Bruce A. Bolt, Academic Press Inc., New York.

Tanimoto, T. and A. Valovcin (2016). Existence of the threshold pressure for seismic excitation by atmospheric disturbances, *Geophys. Res. Lett.*, **43**, doi:10.1002/2016GL070858.

Tanimoto, T. and J. Wang (2018). Low-Frequency Seismic Noise Characteristics From the Analysis of Co-located Seismic and Pressure Data, *J. Geophys. Res., Solid Earth*, 123. https://doi.org/10.1029/2018JB015519

Tanimoto, T. and J. Wang (2019). Theory for deriving shallow elasticity structure from colocated seismic and pressure data, *J. Geophys. Res., Solid Earth*, 124. 5811-5835, https://doi.org/10.1029/2018JB017132

Tytell, J., F. Vernon, M. Hedlin, C. de Groot Hedlin, J. Reyes, B. Busby, K. Hafner, and J. Eakins (2016). The USArray transportable array as a platform for weather observation and research *Bull. Seism. Soc. Am.*, **97**, 603-619, https://doi.org/10.1175/BAMS-D-14-00204.1

UC San Diego (2014). Piñon Flats Observatory Array. International Federation of Digital Seismograph Networks. Dataset/Seismic Network, https://doi.org/10.7914/SN/PY

Vernon, F. L., J. Fletcher, L. Carroll, A. Chave, and E. Sembra (1991). Coherence of seismic body waves from local events as measured by a small-aperture array, *J. Geophys. Res.*, **96**, No. B7, 11981-11996.

Wald, D., and T. Allen (2007), Topographic Slope as a Proxy for Seismic Site Conditions and Amplification, *Bulletin of the Seismological Society of America*, *97*, 1379–1395,doi: 10.1785/0120060267.

Wyatt, F. (1982). Displacement of Surface Monuments: Horizontal Motion, *J. Geophys. Res.*, **87**, No. B2, 979-989.

Yong, A., Thompson, E., Wald, D., Knudsen, K., Odum, J., Stephenson, W., and Haefner, S. (2016). Compilation of Vs30 data for the United States. *U.S. Geological Survey Data Series*, **978**, 8p. https://doi.org/10.3133/ds978

Zalachoris, G., E. M. Rathje, and J. G. Paine (2017). Vs30 Characterization of Texas, Oklahoma, and Kansas using the P-wave Seismogram Method, *Earthquake Spectra*, 33, No. 3, 943-961.

Table 1. Stations in Figure 1. Nine co-located stations from BPH01 to BPH12 below were analyzed for their data from the entire year of 2017. Seismic and pressure sensor types are shown. Data at TPFO are available from November, 2018, thus not included in this study. AZ.PFO is the PFO station in the Anza network and II.PFO is the PFO station in the IDA/IRIS network. Two end points of the linear array, the northwest (NW) point and the southeast (SE) point, are listed. Locations of the borehole sites by Fletcher et al. (1990) are given at bottom. The deep borehole location was used as the site of borehole in Figure 1. Two locations overlap on the scale of this plot.

Station	Latitude (deg)	Longitude (deg)	Altitude (m)	Seismic Inst.	Pres. Inst.
BPH01	33.61100	-116.45550	1292	STS-5A	Setra 278
BPH03	33.61020	-116.45550	1285	Trillium 120	Setra 278
BPH05	33.61250	-116.45520	1302	STS-5A	Setra 278
BPH06	33.61050	-116.45250	1294.	Trillium 120	Setra 278
BPH07	33.60810	-116.45530	1275	Trillium 120	Setra 278
BPH09	33.61260	-116.45990	1295	Trillium 120	Setra 278
BPH10	33.61250	-116.45200	1300	STS-5A	Setra 278
BPH11	33.60550	-116.45190	1300	STS-5A	Setra 278
BPH12	33.60560	-116.46000	1251	Trillium 120	Setra 278
TPFO	33.60600	-116.45440	1275		
AZ.PFO	33.61167	-116.45943	1259		
II.PFO	33.61070	-116.45550	1280		
Array NW end	33.61186	-116.45790	1295		
Array SE end	33.61158	-116.45631	1295		
Deep Borehole	33.61167	-116.45986	1300		
Shallow Borehole	33.61168	-116.46000	1300		

Table 2. Summary of Vs30 estimates. The first row is from Yong et al. (2016) and the second row is from Fletcher et al. (1990). Our results are from the third row with figure numbers (column 4). Cases indicated by X are shown in Figure 15 as the representative Vs30 for each station. Vs30 for each starting model is given in a parenthesis. Uncertainties for Vs30 are one standard deviations except for the borehole value (see text).

Station	Frequency Range (Hz)	Vs30 (m/s)	Figure No.	Selection
USGS (Yong et al. 2016)	High (geophone)	685-840		
Borehole (Fletcher et al. 1990)		702 ± 100		
BPH01	0.005 - 0.030	724 ± 198	S1a	
	0.005 - 0.035	737 ± 198	S1b	
	0.010 - 0.035	$738 \pm 207(776)$	10, S1c	X
BPH03	0.010 - 0.035	$890 \pm 243(862)$	10, S2a	X
	0.005 - 0.035	896 ± 261	S2b	
	0.010 - 0.040	921 ± 252	S2c	
BPH05	0.010 - 0.035	$979 \pm 261(957)$	10, S3a	X
	0.005 - 0.035	981 ± 264	S3b	
	0.005 - 0.045	995 ± 270	S3c	
BPH06	0.015 - 0.035	1489 ± 395	S4a	
	0.015 - 0.040	$1549 \pm 404(1613)$	11, S4b	X
	0.010 - 0.040	1548 ± 395	S4c	
BPH07	0.010 - 0.035	$627 \pm 165(639)$	11, S5a	X
	0.005 - 0.035	628 ± 162	S5b	
	0.005 - 0.045	633 ± 180	S5c	
BPH09	0.005 - 0.030	995 ± 270	S6a	
	0.005 - 0.035	982 ± 261	S6b	
	0.010 - 0.040	$975 \pm 261(979)$	11, S6c	X
BPH10	0.010 - 0.035	$1159 \pm 315(1168)$	12, S7a	X
	0.010 - 0.040	1179 ± 333	S7b	
	0.005 - 0.035	1164 ± 324	S7c	
BPH11	0.010 - 0.040	$603 \pm 162(632)$	12, S8a	X
	0.005 - 0.040	606 ± 156	S8b	
	0.005 - 0045	596 ± 148	S8c	
BPH12	0.015 - 0.035	1359 ± 360	S9a	
	0.015 - 0.040	1370 ± 384	S9b	
	0.010 - 0.040	$1368 \pm 378(1326)$	12, S9c	X

Table 3. Measurements for BPH01. Ratios S_z/S_p and S_H/S_p, pressure-wave speed c, and $\overline{\mu}$

Freq. (Hz)	S_z/S_p $(m^2/s^2/Pa^2)$	S_H/S_p $(m^2/s^2/Pa^2)$	c (m/s)	$\bar{\mu}$ (Pa)
0.010	7.726e-19 (± 6.107e-19)	4.177e-15 (± 3.109e-15)	2.121e+00 (± 1.152e+00)	1.207e+09 (± 4.491e+08)
0.015	7.902e-19 (± 6.463e-19)	2.065e-15 (± 1.250e-15)	2.034e+00 (± 1.035e+00)	1.144e+09 (± 3.463e+08)
0.020	1.161e-18 (± 9.093e-19)	1.301e-15 (± 1.006e-15)	2.330e+00 (± 1.282e+00)	1.081e+09 (± 4.180e+08)
0.025	1.183e-18 (± 9.169e-19)	8.583e-16 (± 6.122e-16)	2.317e+00 (± 1.220e+00)	1.065e+09 (± 3.798e+08)
0.030	1.015e-18 (± 7.942e-19)	8.023e-16 (± 6.841e-16)	1.849e+00 (± 1.070e+00)	9.178e+08 (± 3.913e+08)
0.035	1.291e-18 (± 9.353e-19)	3.888e-16 (± 2.332e-16)	2.568e+00 (± 1.207e+00)	1.130e+09 (± 3.388e+08)

Table 4. Measurements for BPH03

Freq. (Hz)	S_z/S_p $(m^2/s^2/Pa^2)$	S_H/S_p $(m^2/s^2/Pa^2)$	c (m/s)	$\bar{\mu}$ (Pa)
0.010	1.316e-18 (± 7.083e-19)	4.607e-15 (± 2.668e-15)	2.636e+00 (± 1.042e+00)	1.149e+09 (± 3.327e+08)
0.015	1.058e-18 (± 6.083e-19)	1.577e-15 (± 8.722e-16)	2.694e+00 (± 1.074e+00)	1.309e+09 (± 3.621e+08)
0.020	1.520e-18 (± 9.008e-19)	8.874e-16 (± 5.211e-16)	3.227e+00 (± 1.346e+00)	1.309e+09 (± 3.843e+08)
0.025	1.860e-18 (± 1.107e-18)	6.690e-16 (± 4.096e-16)	3.290e+00 (± 1.404e+00)	1.206e+09 (± 3.692e+08)
0.030	1.915e-18 (± 1.021e-18)	3.552e-16 (± 2.132e-16)	3.818e+00 (± 1.532e+00)	1.379e+09 (± 4.139e+08)
0.035	2.244e-18 (± 1.546e-18)	2.385e-16 (± 1.654e-16)	4.323e+00 (± 2.113e+00)	1.443e+09 (± 5.002e+08)

Table 5. Measurements for BPH05

Freq. (Hz)	S_z/S_p $(m^2/s^2/Pa^2)$	S_H/S_p $(m^2/s^2/Pa^2)$	c (m/s)	$\bar{\mu}$ (Pa)
0.010	7.544e-19 (± 4.671e-19)	2.375e-15 (± 1.133e-15)	2.780e+00 (± 1.086e+00)	1.600e+09 (± 3.817e+08)
0.015	1.162e-18 (± 6.919e-19)	1.168e-15 (± 5.595e-16)	3.279e+00 (± 1.253e+00)	1.521e+09 (± 3.643e+08)
0.020	1.383e-18 (± 9.256e-19)	5.445e-16 (± 3.264e-16)	3.931e+00 (± 1.765e+00)	1.671e+09 (± 5.007e+08)
0.025	1.805e-18 (± 1.184e-18)	3.736e-16 (± 2.309e-16)	4.337e+00 (± 1.954e+00)	1.614e+09 (± 4.988e+08)
0.030	2.198e-18 (± 1.877e-18)	2.481e-16 (± 1.497e-16)	4.893e+00 (± 2.559e+00)	1.650e+09 (± 4.980e+08)
0.035	2.766e-18 (± 1.983e-18)	1.740e-16 (± 1.014e-16)	5.619e+00 (± 2.595e+00)	1.689e+09 (± 4.920e+08)

Table 6. Measurements for BPH06

Freq. (Hz)	S_z/S_p $(m^2/s^2/Pa^2)$	S_H/S_p $(m^2/s^2/Pa^2)$	c (m/s)	$\bar{\mu}$ (Pa)
0.015	1.835e-19 (± 1.299e-19)	1.054e-16 (± 6.012e-17)	4.338e+00 (± 1.972e+00)	5.064e+09 (± 1.444e+09)
0.020	1.927e-19 (± 1.176e-19)	5.555e-17 (± 3.654e-17)	4.593e+00 (± 2.060e+00)	5.232e+09 (± 1.721e+09)
0.025	1.986e-19 (± 1.273e-19)	4.520e-17 (± 3.395e-17)	4.135e+00 (± 2.042e+00)	4.640e+09 (± 1.743e+09)
0.030	2.413e-19 (± 1.575e-19)	3.584e-17 (± 2.553e-17)	4.266e+00 (± 2.061e+00)	4.342e+09 (± 1.546e+09)
0.035	2.796e-19 (± 1.857e-19)	2.668e-17 (± 1.942e-17)	4.562e+00 (± 2.248e+00)	4.314e+09 (± 1.570e+09)
0.040	3.287e-19 (± 2.111e-19)	1.614e-17 (± 1.302e-17)	5.565e+00 (± 2.870e+00)	4.854e+09 (± 1.959e+09)

Table 7. Measurements for BPH07

Freq. (Hz)	S_z/S_p $(m^2/s^2/Pa^2)$	S_H/S_p $(m^2/s^2/Pa^2)$	c (m/s)	$\bar{\mu}$ (Pa)
0.010	9.348e-19 (± 4.625e-19)	9.028e-15 (± 6.701e-15)	1.587e+00 (± 7.078e-01)	8.208e+08 (± 3.046e+08)
0.015	7.334e-19 (± 4.789e-19)	4.584e-15 (± 2.473e-15)	1.315e+00 (± 5.570e-01)	7.679e+08 (± 2.071e+08)
0.020	6.750e-19 (± 4.298e-19)	2.888e-15 (± 2.153e-15)	1.192e+00 (± 5.844e-01)	7.256e+08 (± 2.704e+08)
0.025	8.946e-19 (± 5.490e-19)	2.054e-15 (± 1.446e-15)	1.302e+00 (± 6.079e-01)	6.883e+08 (± 2.422e+08)
0.030	1.228e-18 (± 8.713e-19)	1.404e-15 (± 1.010e-15)	1.538e+00 (± 7.767e-01)	6.937e+08 (± 2.495e+08)
0.035	1.374e-18 (± 1.005e-18)	1.011e-15 (± 6.278e-16)	1.643e+00 (± 7.880e-01)	7.006e+08 (± 2.175e+08)

Table 8. Measurements for BPH09

Freq. (Hz)	S_z/S_p $(m^2/s^2/Pa^2)$	S_H/S_p $(m^2/s^2/Pa^2)$	c (m/s)	$\bar{\mu}$ (Pa)
0.010	5.456e-19 (± 3.391e-19)	1.892e-15 (± 8.709e-16)	2.649e+00 (± 1.024e+00)	1.793e+09 (± 4.127e+08)
0.015	7.717e-19 (± 4.368e-19)	8.624e-16 (± 4.054e-16)	3.110e+00 (± 1.144e+00)	1.770e+09 (± 4.161e+08)
0.020	7.266e-19 (± 5.175e-19)	4.739e-16 (± 2.886e-16)	3.054e+00 (± 1.431e+00)	1.791e+09 (± 5.454e+08)
0.025	1.042e-18 (± 5.213e-19)	3.247e-16 (± 1.899e-16)	3.535e+00 (± 1.360e+00)	1.731e+09 (± 5.062e+08)
0.030	9.032e-19 (± 7.466e-19)	2.069e-16 (± 1.135e-16)	3.435e+00 (± 1.704e+00)	1.807e+09 (± 4.957e+08)
0.035	1.116e-18 (± 6.921e-19)	1.646e-16 (± 9.177e-17)	3.669e+00 (± 1.530e+00)	1.737e+09 (± 4.842e+08)
0.040	1.853e-18 (± 1.471e-18)	1.289e-16 (± 7.725e-17)	4.675e+00 (± 2.324e+00)	1.717e+09 (± 5.144e+08)

Table 9. Measurements for BPH10

Freq. (Hz)	S_z/S_p $(m^2/s^2/Pa^2)$	S_H/S_p $(m^2/s^2/Pa^2)$	c (m/s)	$\bar{\mu}$ (Pa)
0.010	4.810e-19 (± 3.403e-19)	8.436e-16 (± 4.423e-16)	3.724e+00 (± 1.640e+00)	2.685e+09 (± 7.039e+08)
0.015	4.322e-19 (± 3.506e-19)	4.425e-16 (± 2.601e-16)	3.249e+00 (± 1.628e+00)	2.471e+09 (± 7.263e+08)
0.020	3.775e-19 (± 3.028e-19)	2.627e-16 (± 1.865e-16)	2.956e+00 (± 1.584e+00)	2.406e+09 (± 8.542e+08)
0.025	3.837e-19 (± 2.804e-19)	1.739e-16 (± 1.334e-16)	2.931e+00 (± 1.553e+00)	2.366e+09 (± 9.076e+08)
0.030	5.699e-19 (± 4.546e-19)	9.974e-17 (± 6.856e-17)	3.930e+00 (± 2.069e+00)	2.603e+09 (± 8.945e+08)
0.035	5.212e-19 (± 3.550e-19)	8.402e-17 (± 4.457e-17)	3.510e+00 (± 1.515e+00)	2.431e+09 (± 6.447e+08)

Table 10. Measurements for BPH11

Freq. (Hz)	S_z/S_p $(m^2/s^2/Pa^2)$	S_H/S_p $(m^2/s^2/Pa^2)$	c (m/s)	$\bar{\mu}$ (Pa)
0.010	2.006e-18 (± 9.451e-19)	7.903e-15 (± 4.330e-15)	2.485e+00 (± 8.978e-01)	8.773e+08 (± 2.403e+08)
0.015	2.374e-18 (± 1.084e-18)	4.048e-15 (± 2.258e-15)	2.518e+00 (± 9.078e-01)	8.172e+08 (± 2.280e+08)
0.020	3.187e-18 (± 1.336e-18)	2.722e-15 (± 1.289e-15)	2.668e+00 (± 8.439e-01)	7.474e+08 (± 1.769e+08)
0.025	4.471e-18 (± 1.797e-18)	1.837e-15 (± 1.001e-15)	3.077e+00 (± 1.041e+00)	7.277e+08 (± 1.982e+08)
0.030	5.124e-18 (± 3.204e-18)	1.298e-15 (± 7.484e-16)	3.267e+00 (± 1.390e+00)	7.216e+08 (± 2.081e+08)
0.035	6.683e-18 (± 3.359e-18)	1.032e-15 (± 6.375e-16)	3.587e+00 (± 1.429e+00)	6.937e+08 (± 2.144e+08)
0.040	6.143e-18 (± 3.465e-18)	7.107e-16 (± 4.508e-16)	3.625e+00 (± 1.539e+00)	7.313e+08 (± 2.320e+08)

Table 11. Measurements for BPH12

Freq. (Hz)	S_z/S_p $(m^2/s^2/Pa^2)$	S_H/S_p $(m^2/s^2/Pa^2)$	c (m/s)	$\bar{\mu}$ (Pa)
0.010	3.843e-19 ($\pm$ 2.504e-19)	6.712e-16 ($\pm$ 3.449e-16)	3.732e+00 ($\pm$ 1.548e+00)	3.010e+09 ($\pm$ 7.733e+08)
0.015	3.154e-19 ($\pm$ 2.421e-19)	2.928e-16 ($\pm$ 1.835e-16)	3.413e+00 ($\pm$ 1.691e+00)	3.039e+09 ($\pm$ 9.525e+08)
0.020	3.023e-19 ($\pm$ 2.045e-19)	2.067e-16 ($\pm$ 1.365e-16)	2.982e+00 ($\pm$ 1.410e+00)	2.712e+09 ($\pm$ 8.958e+08)
0.025	3.041e-19 ($\pm$ 1.873e-19)	1.104e-16 ($\pm$ 6.897e-17)	3.274e+00 ($\pm$ 1.437e+00)	2.969e+09 ($\pm$ 9.275e+08)
0.030	3.498e-19 ($\pm$ 2.047e-19)	7.974e-17 ($\pm$ 4.206e-17)	3.444e+00 ($\pm$ 1.356e+00)	2.911e+09 ($\pm$ 7.677e+08)
0.035	2.987e-19 ($\pm$ 2.027e-19)	4.315e-17 ($\pm$ 2.181e-17)	3.708e+00 ($\pm$ 1.569e+00)	3.392e+09 ($\pm$ 8.572e+08)
0.040	3.840e-19 ($\pm$ 2.772e-19)	3.584e-17 ($\pm$ 2.258e-17)	4.036e+00 ($\pm$ 1.934e+00)	3.257e+09 ($\pm$ 1.026e+09)

FIGURE CAPTIONS

Figure 1: Piñon Flat Observatory (rectangle) and surrounding area. Elevations are indicated by colors.

Figure 2: Map of stations in the Piñon Flat Observatory. Numbers from 1 to 13 denote stations from BPH01 to BPH13. Nine stations indicated by blue circles are stations with pressure and seismic sensors, also listed in Table 1. Open circles are stations with seismic instruments only. The green circle is station PFO in the Anza network (network code AZ) and the pink circle is PFO in the IDA-IRIS network (network code II). The red line is the location of linear geophone array by Yong et al. (2016), also referred to as the USGS study in this paper. The red circle was the site of borehole study by Fletcher et al. (1990). The location of BPH01 is defined as the origin.

Figure 3: Nine colocated stations have one of the two types of seismic sensors, STS-5A or Trillium 120. Normalized amplitude response curves are shown (normalized at 0.1 Hz).

Figure 4: (left) Pressure-seismic plot for station KMSC (South Carolina), one of the EarthScope TA station. Seismic PSDs (blue for vertical data and red for horizontal data) are plotted against pressure PSDs. For vertical data, the threshold pressure is at about 1 (Pa^2/Hz), above which seismic amplitudes (PSD) become proportional to pressure amplitude. Below this threshold pressure, vertical amplitudes are relatively constant, indicating that seismic noise is irrelevant of local pressure changes. Green points indicate high-coherence data between pressure and seismic data with coherence higher than 0.8. (right) For pressure above the threshold pressure, vertical seismic data basically show pressure loading effects.

Figure 5: In a high pressure range, when coherence is high, phase differences between pressure and seismic vertical displacement are about 180 degrees. If they are at 180 degrees, pressure and surface vertical displacements have the relationship, as illustrated in the top panel. It shows the pressure-loading effects on the surface; when pressure is high, the surface is pushed down and vice versa.

Figure 6: Two examples of measurements, S_z/S_p and S_H/S_p, for station BPH11 at 0.015 Hz (a and b) and at 0.035 Hz (c and d). a and c are pressure-seismic plots; blue are vertical data, red are horizontal data and green are high-coherence points above 0.7. For measuring the ratios between seismic PSDs and pressure PSDs, we plot S_z/S_p and S_H/S_p against S_p. High coherence data should approach constant values at high pressure. We select points, indicated by boxes, and compute the average and standard deviations.

Figure 7: Pressure-seismic plots for all nine stations at 0.02 Hz. Green points are from the one-hour

time intervals when coherence between pressure and seismic data is higher than 0.6. The numbers of high-coherence (green) points vary from station to station.

Figure 8: An example of inversion procedure for BPH11. (a) Variances decrease quickly with each iteration step. We chose the second solution as the final solution in this study. (b) Measured data are from 0.01 Hz to 0.04 Hz at an interval of 0.005 Hz. (c) Depth variations of shear modulus (left) and bulk modulus (right) are shown. Blue is for the starting model, green is the first iteration model and red is the second iteration model. (d) Using the density model (green), derived from empirical relations, we converted shear modulus and bulk modulus to density, P-wave, and S-wave speeds. Vs30 is computed from S-wave speeds from this profile.

Figure 9: The shear-modulus kernels (top) and the bulk-modulus kernels (bottom) in the integrand of (4) or (5). They are for BPH11 from the first iteration step. The shear-modulus kernels are much larger than the bulk-modulus kernels. These kernels do not change very much with iteration steps.

Figure 10: Selected cases of inversion for BPH01 (left), BPH03 (middle) and BPH05 (right). They are marked by X in Table 2. For each station, the fit to data is shown in the top panel, shear-modulus (left) and bulk-modulus structures (right) are in the middle panels and density, P-wave and S-wave speeds are in the bottom panel. Unit for S_z/S_H is $m^2/s^2/Pa^2$.

Figure 11: Selected cases of inversion for BPH06 (left), BPH07 (middle) and BPH09 (right). Otherwise, same with Figure 10.

Figure 12: Selected cases of inversion for BPH10 (left), BPH11 (middle) and BPH12 (right). Otherwise, same with Figure 10.

Figure 13: Depth resolution kernels for nine cases of inversions. They correspond to the cases in Figures 10-12.

Figure 14: Comparison of the shear-modulus structures for BPH01, BPH03, BPH05, and BPH09 against three models in Yong et al. (2016). Among their models, two Rayleigh-wave results (MASW, Poisson's ratio 0.2 and 0.3) and one Love-wave result (MALW) are shown. Their models were converted to shear-modulus structures. Our results are very smooth in comparison to their models. Vs30 values are still close, shown in parentheses in unit of m/s.

Figure 15: Our estimates of Vs30 for the nine colocated stations compared against Vs30 by Yong et al. (2016) and Vs30 at the borehole based on S-wave speed model in Fletcher et al. (1990). The numbers

by blue circles are the station numbers (1 is for BPH01, 3 for BPH03 and so forth). The numbers in parentheses are our estimates for Vs30 in m/s.

Figure 16: S-wave speed model by Fletcher et al. (1990). Vs30 was computed by integrating this structure in the upper 30 m (Vs30 = 702 m/s).

Figure S1: Three cases of inversion for BPH01. The frequency ranges are (a) 0.01-0.035 Hz, (b) 0.005-0.035 Hz, and (c) 0.01-0.04 Hz. Otherwise, same with Figure 10.

Figure S2: Three cases of inversion for BPH03. The frequency ranges are (a) 0.01-0.035 Hz, (b) 0.005-0.035 Hz, and (c) 0.01-0.04 Hz. Otherwise, same with Figure 10.

Figure S3: Three cases of inversion for BPH05. The frequency ranges are (a) 0.01-0.035 Hz, (b) 0.005-0.035 Hz, and (c) 0.005-0.045 Hz. Otherwise, same with Figure 10.

Figure S4 Three cases of inversion for BPH06. The frequency ranges are (a) 0.010-0.035 Hz, (b) 0.015-0.040 Hz, and (c) 0.005-0.040 Hz. Otherwise, same with Figure 10.

Figure S5: Three cases of inversion for BPH07. The frequency ranges are (a) 0.01-0.035 Hz, (b) 0.005-0.035 Hz, and (c) 0.005-0.045 Hz. Otherwise, same with Figure 10.

Figure S6: Three cases of inversion for BPH09. The frequency ranges are (a) 0.005-0.030 Hz, (b) 0.005-0.035 Hz, and (c) 0.01-0.04 Hz. Otherwise, same with Figure 10.

Figure S7: Three cases of inversion for BPH10. The frequency ranges are (a) 0.010-0.035 Hz, (b) 0.010-0.040 Hz, and (c) 0.005-0.035 Hz. Otherwise, same with Figure 10.

Figure S8: Three cases of inversion for BPH11. The frequency ranges are (a) 0.01-0.040 Hz, (b) 0.005-0.040 Hz, and (c) 0.005-0.045 Hz. Otherwise, same with Figure 10.

Figure S9: Three cases of inversion for BPH12. The frequency ranges are (a) 0.015-0.035 Hz, (b) 0.015-0.040 Hz, and (c) 0.010-0.040 Hz. Otherwise, same with Figure 10.

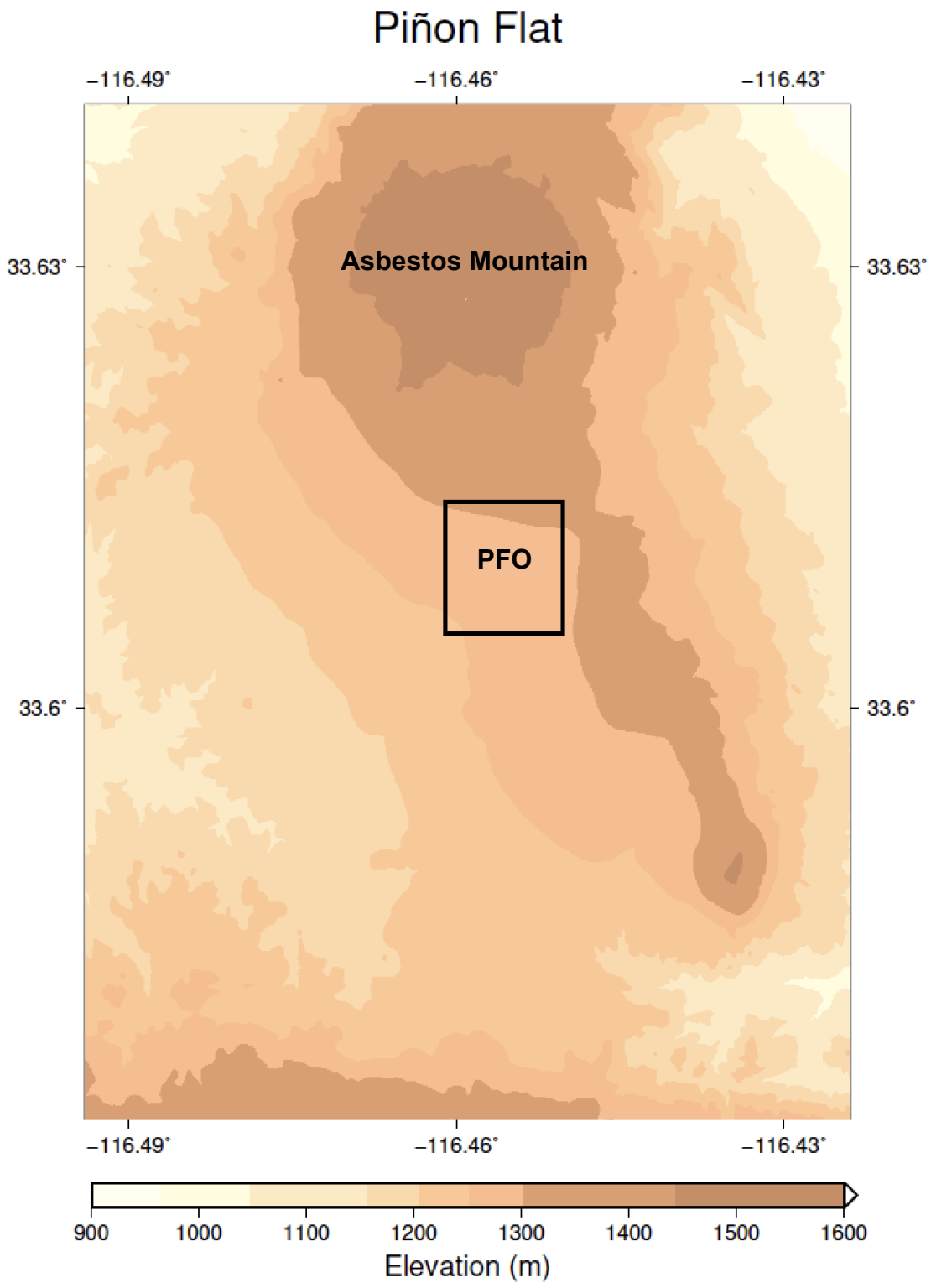

Figure 1: Pinyon Flat Observatory (rectangle) and surrounding area. Elevations are indicated by colors.

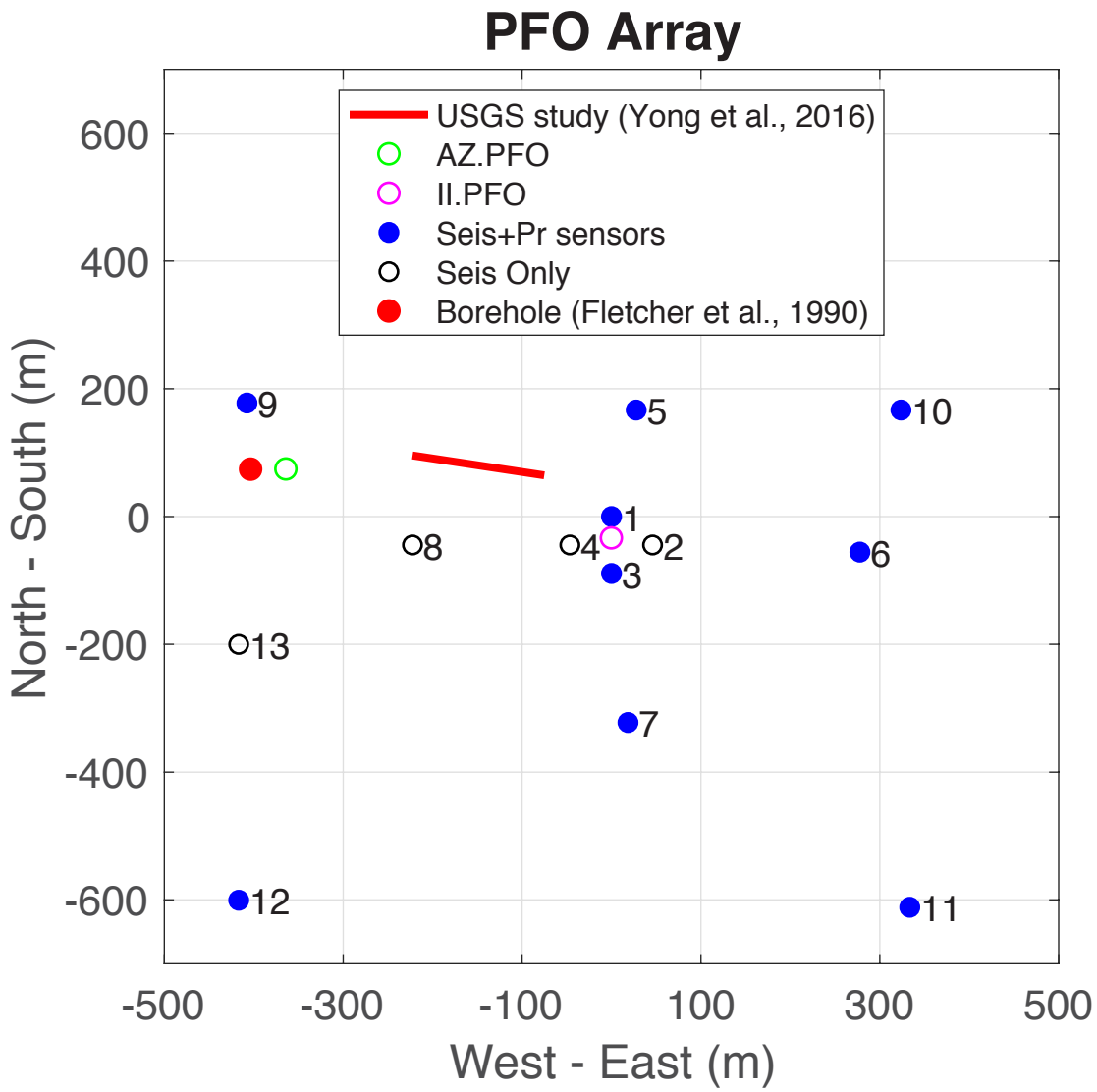

Figure 2: Map of stations in the Pinyon Flat Observatory. Numbers from 1 to 13 denote stations from BPH01 to BPH13. Nine stations indicated by blue circles are stations with pressure and seismic sensors, also listed in Table 1. Open circles are stations with seismic instruments only. Green circle is station PFO in the Anza network (network code AZ) and pink circle id PFO in the IDA-IRIS network (network code II). The red line is the location of linear geophone array by Yong et al. (2016), also referred to as the USGS study in this paper. The red circle was the site of borehole study by Fletcher et al. (1990). The location of BPH01 is defined as the origin.

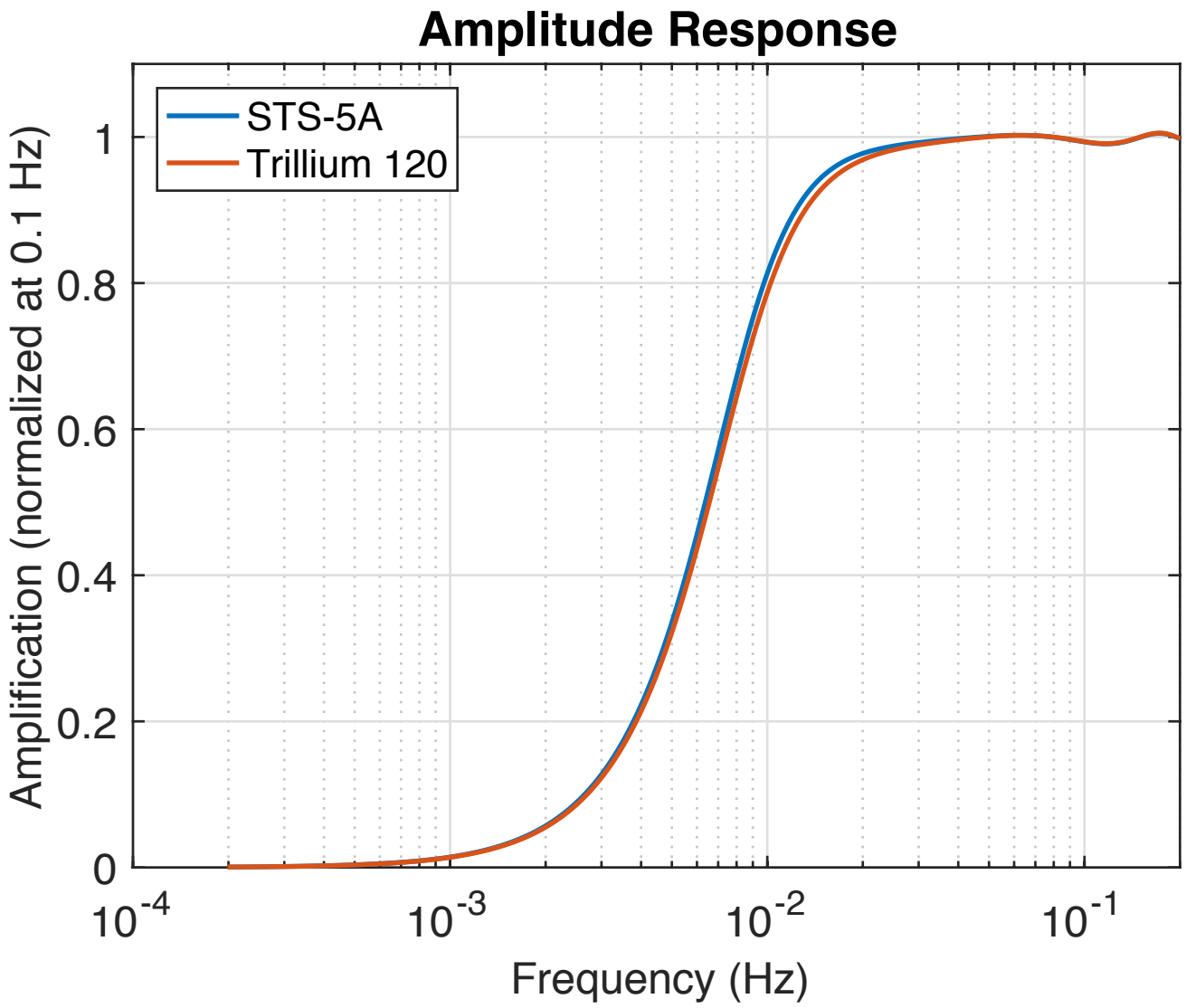

Figure 3: Nine colocated stations have one of the two types of seismic sensors, STS-5A or Trillium 120. Normalized amplitude response curves are shown (both normalized at 0.1 Hz).

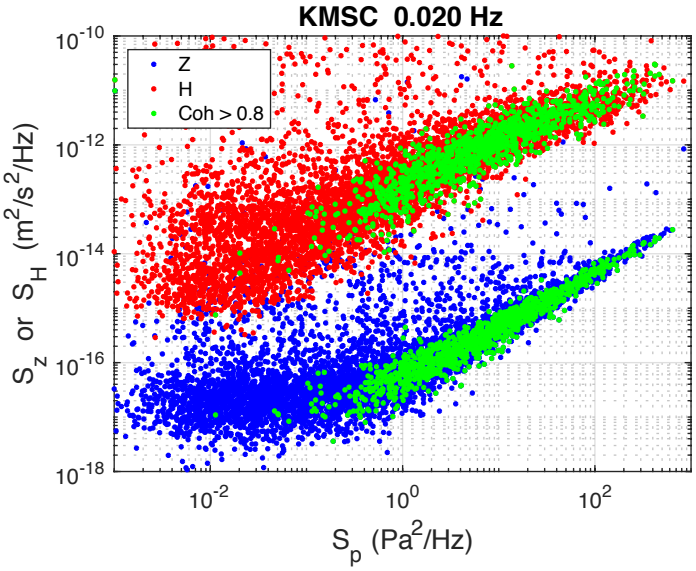

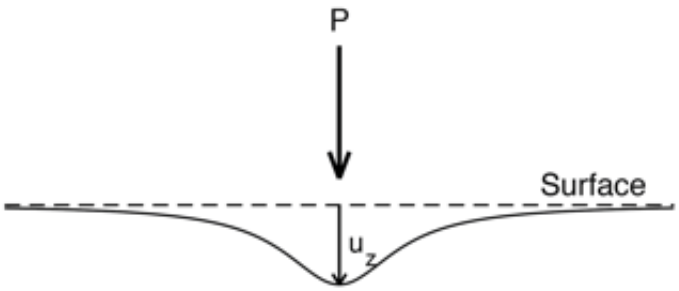

Figure 4: (left) Pressure-seismic plot for station KMSC (South Carolina), one of the Earth-Scope TA station. Seismic PSDs (blue cirlces are vertical data and red circles are horizontal data). For vertical data, the threshold pressure is at about 1 (Pa**2/Hz), above which seismic amplitudes (PSD) become proportional to local pressure. Below this pressure, vertical amplitudes are constant, indicating that seismic noise is irrelevant of local pressure changes. Green points are the one-hour-long time intervals for which coherence between pressure and seismic data are higher than 0.8. (right) For pressure above the threshold pressure, vertical seismic data basically show pressure loading effects.

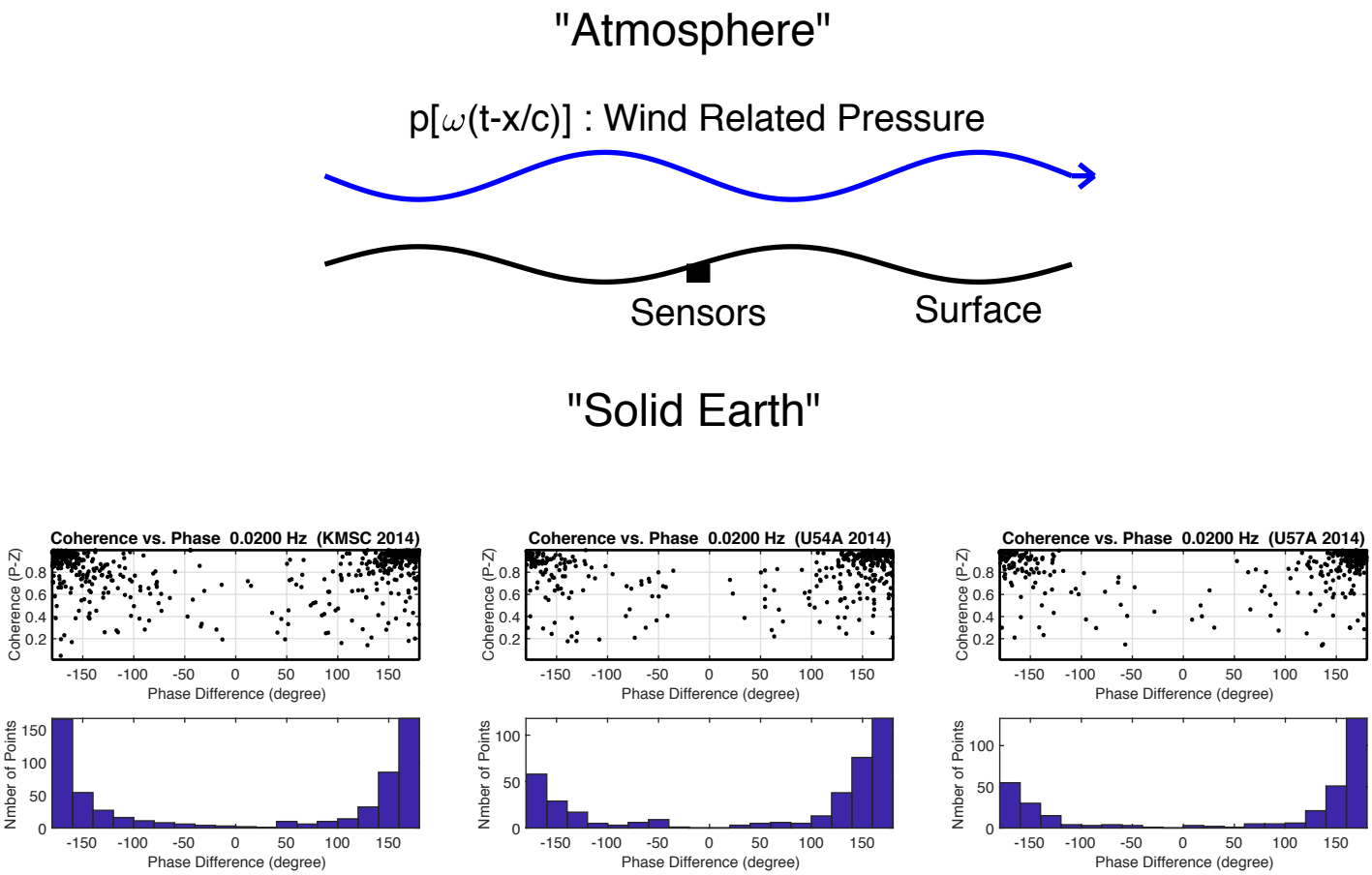

Figure 5: In a high pressure range, when coherence is high, phase differences between pressure and vertical displacement are about 180 degrees. If they are at 180 degrees, pressure and surface vertical displacements have the relationship, as illustrated in the top panel. It shows the pressure-loading effects on the surface, as when pressure is high, the surface is pushed down and vice versa.

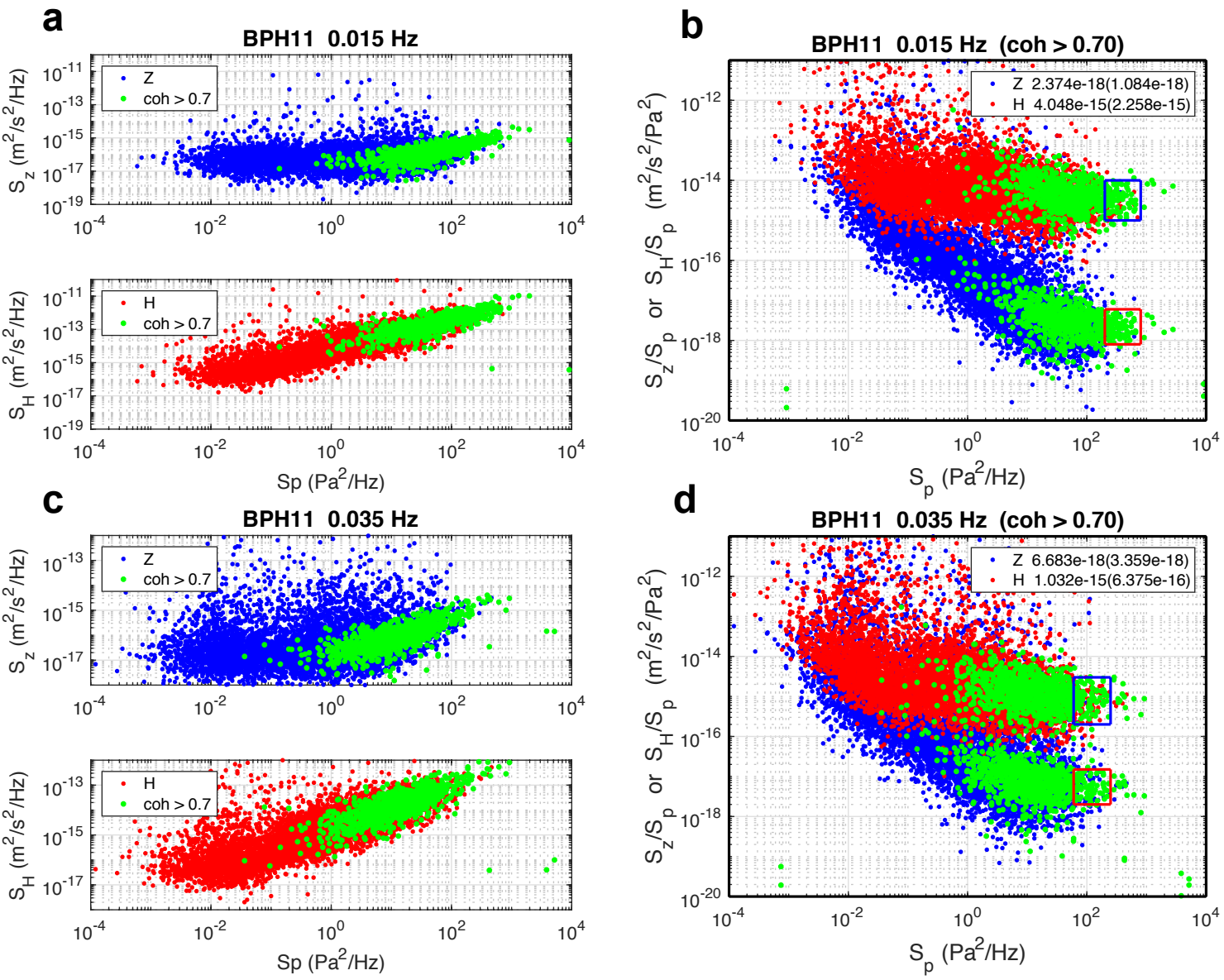

Figure 6: Two examples of measurements, Sz/Sp and SH/Sp, for station BPH11 at 0.015 Hz (a and b) and at 0.035 Hz (c and d). a and c are pressure-seismic plots (blue data are vertical data, red data are horizontal data with high coherence points (above 0.7) are shown by green points. For the measurements of the ratios, we first plot Sz/Sp and SH/Sp against Sp. High coherence data should approach constant values for high pressure. We select points, indicated by boxes, and calculate the means and standard deviations.

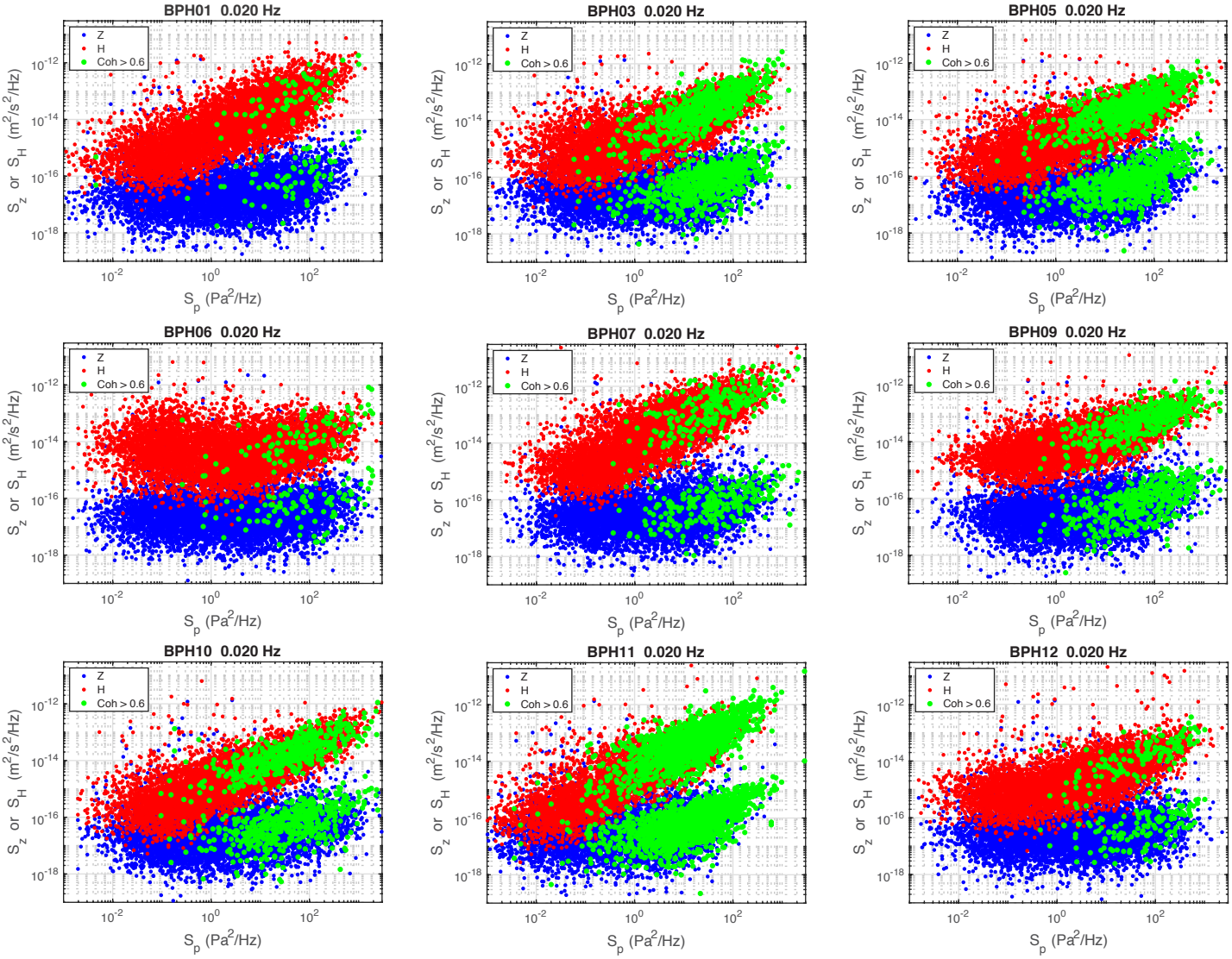

Figure 7: Pressure-seismic plots for all nine stations at 0.02 Hz. Green points are from the one-hour time intervals when coherence between pressure and seismic data is higher than 0.6. The numbers of high-coherence (green) points vary from station to station.

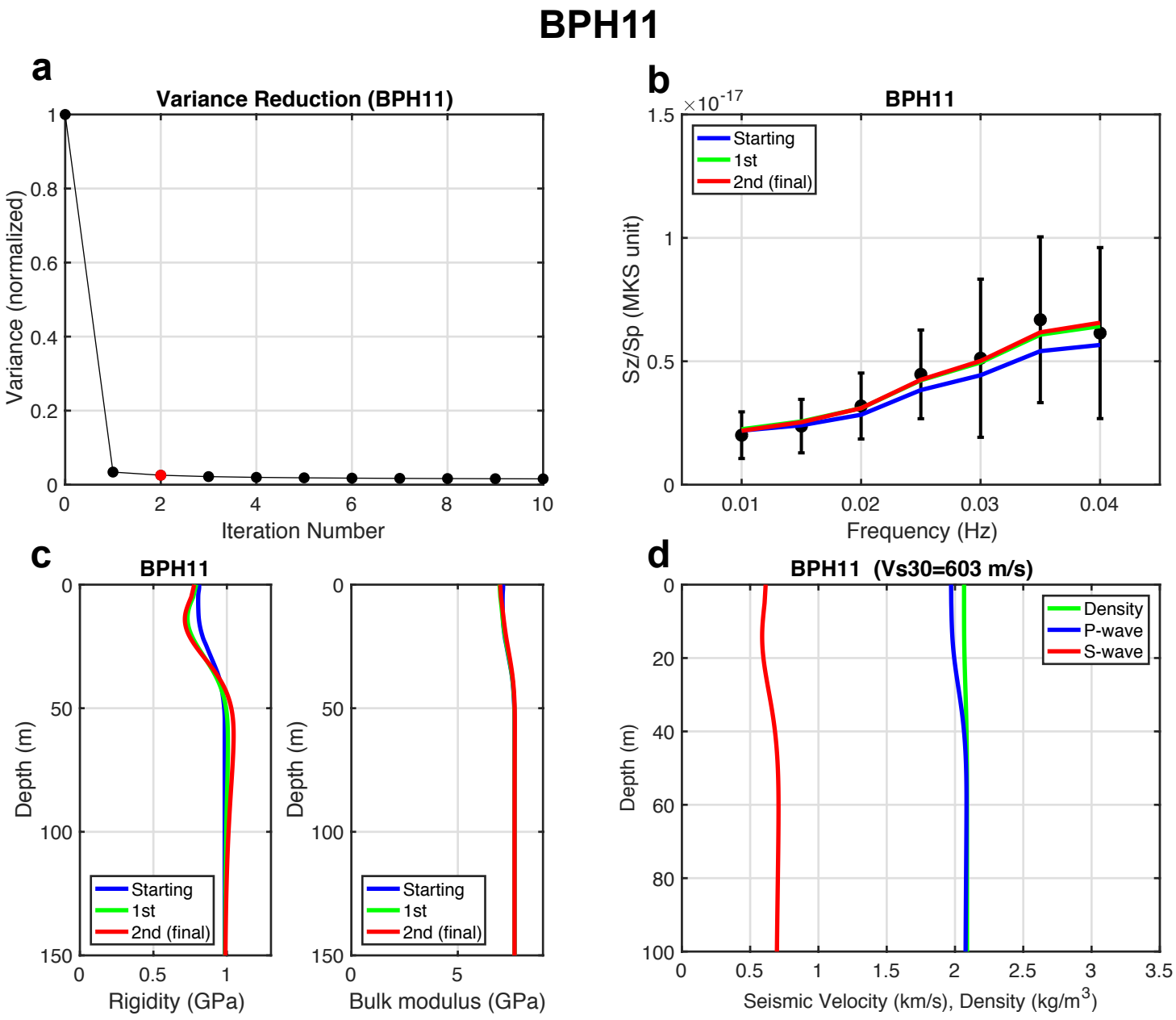

Figure 8: An example of inversion procedure for BPH11. (a) Variances decrease rapidly with iteration steps. We chose the second solution as the final solution in this study. (b) Measured data are from 0.01 Hz to 0.04 Hz at an interval of 0.005 Hz. (c) Depth variation of rigidity (left) and bulk modulus (right) for the starting model (blue), the first iteration model (green) and the second iteration model (red). (d) Using the density model (green), derived from empirical relations, we converted shear and bulk modulus solutions to density, P-wave, and S-wave speeds structures. Vs30 is computed from S-wave speeds from this profile.

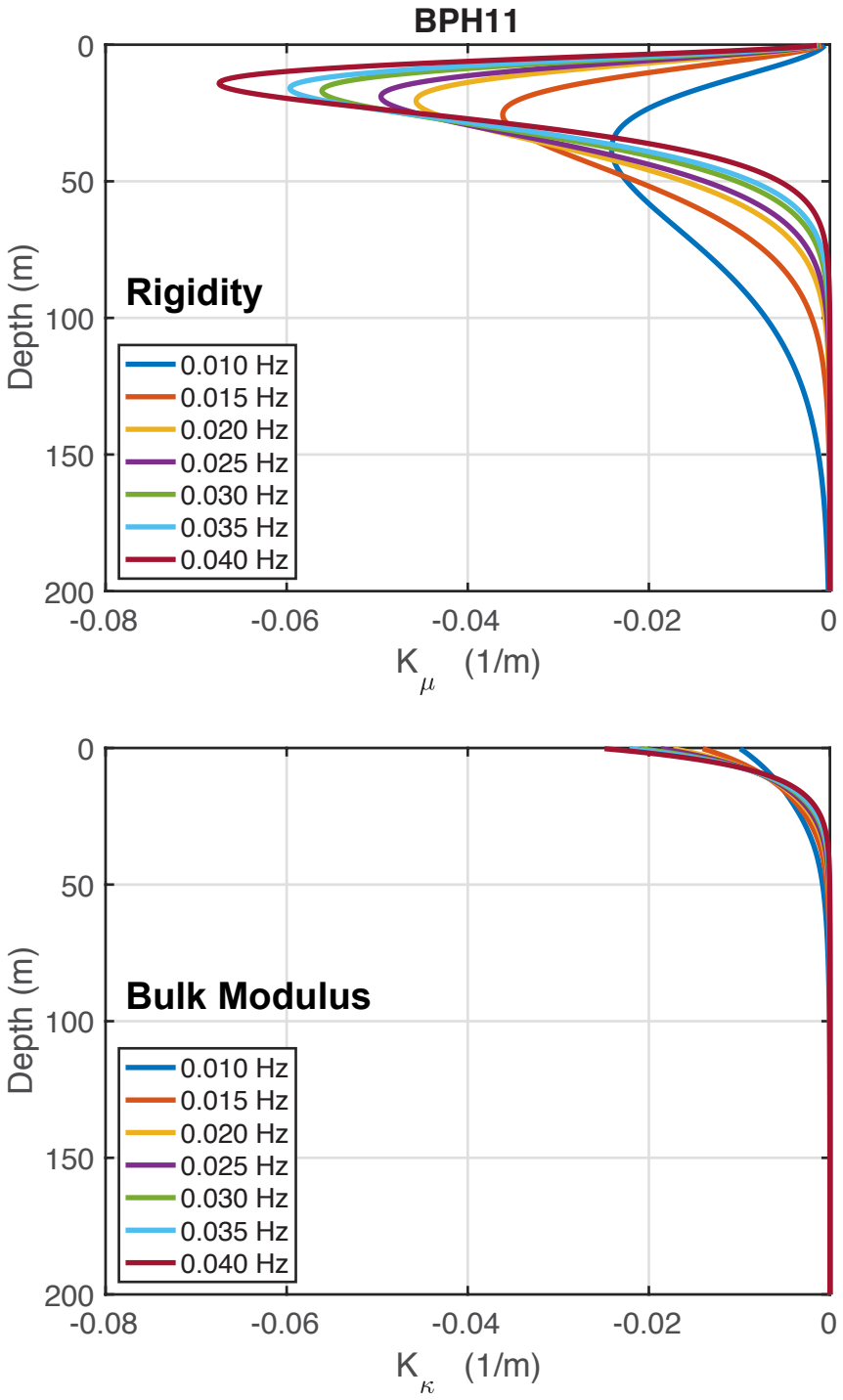

Figure 9: The shear-modulus kernels (top) and the bulk-modulus kernels (bottom) in the integrand of (4) or (5). They are for BPH11 from the first iteration step. The shear-modulus kernels are much larger than the bulk-modulus kernels. These kernels do not change very much with iterations.

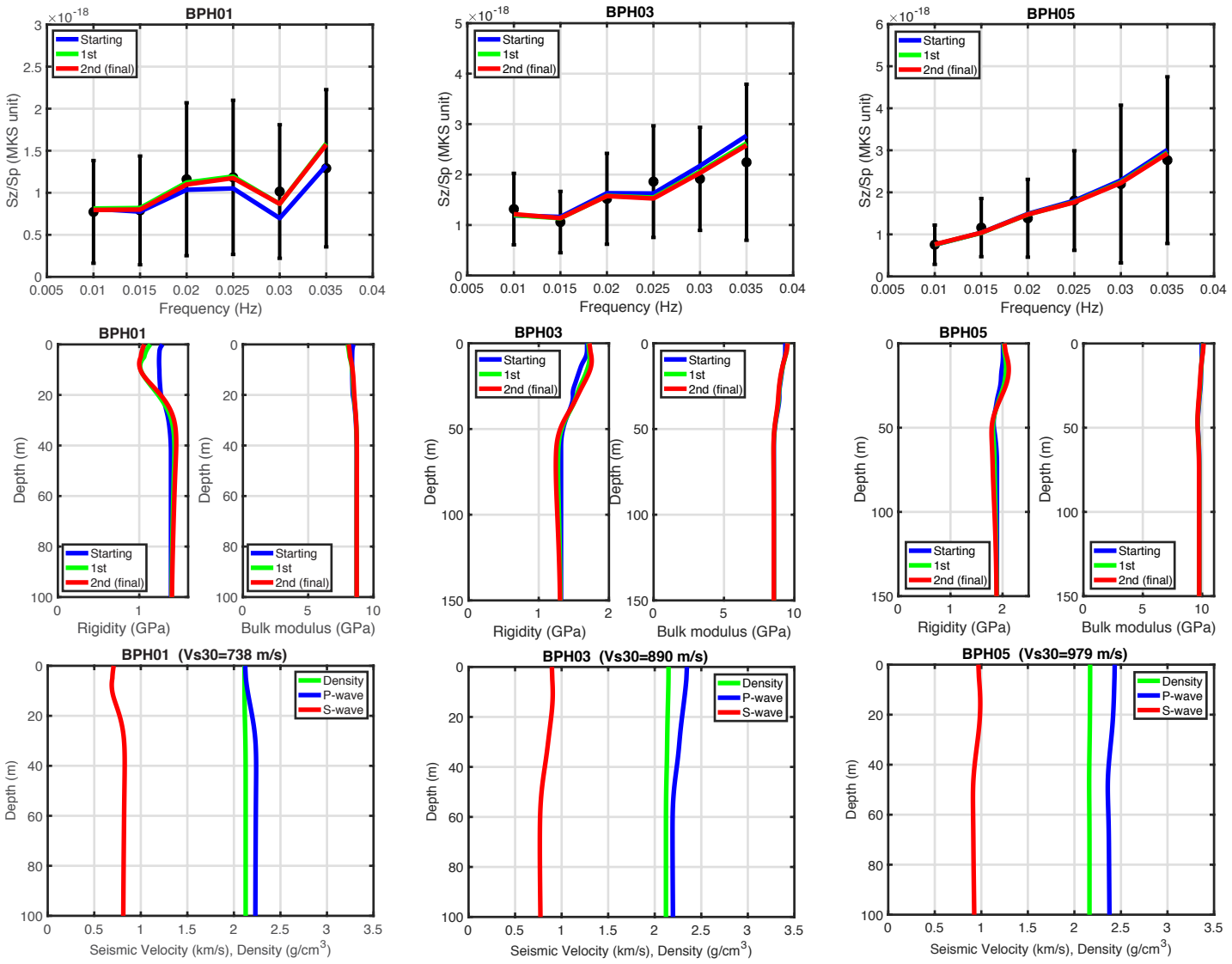

Figure 10: Selected cases of inversion for BPH01 (left), BPH03 (middle) and BPH05 (right). They are marked by X in Table 2. For each station, fit to data are shown in the top panel, shear-modulus structures (left) and bulk-modulus structures (right) are in the middle panels and density, P-wave and S-wave speeds are in the bottom panel.

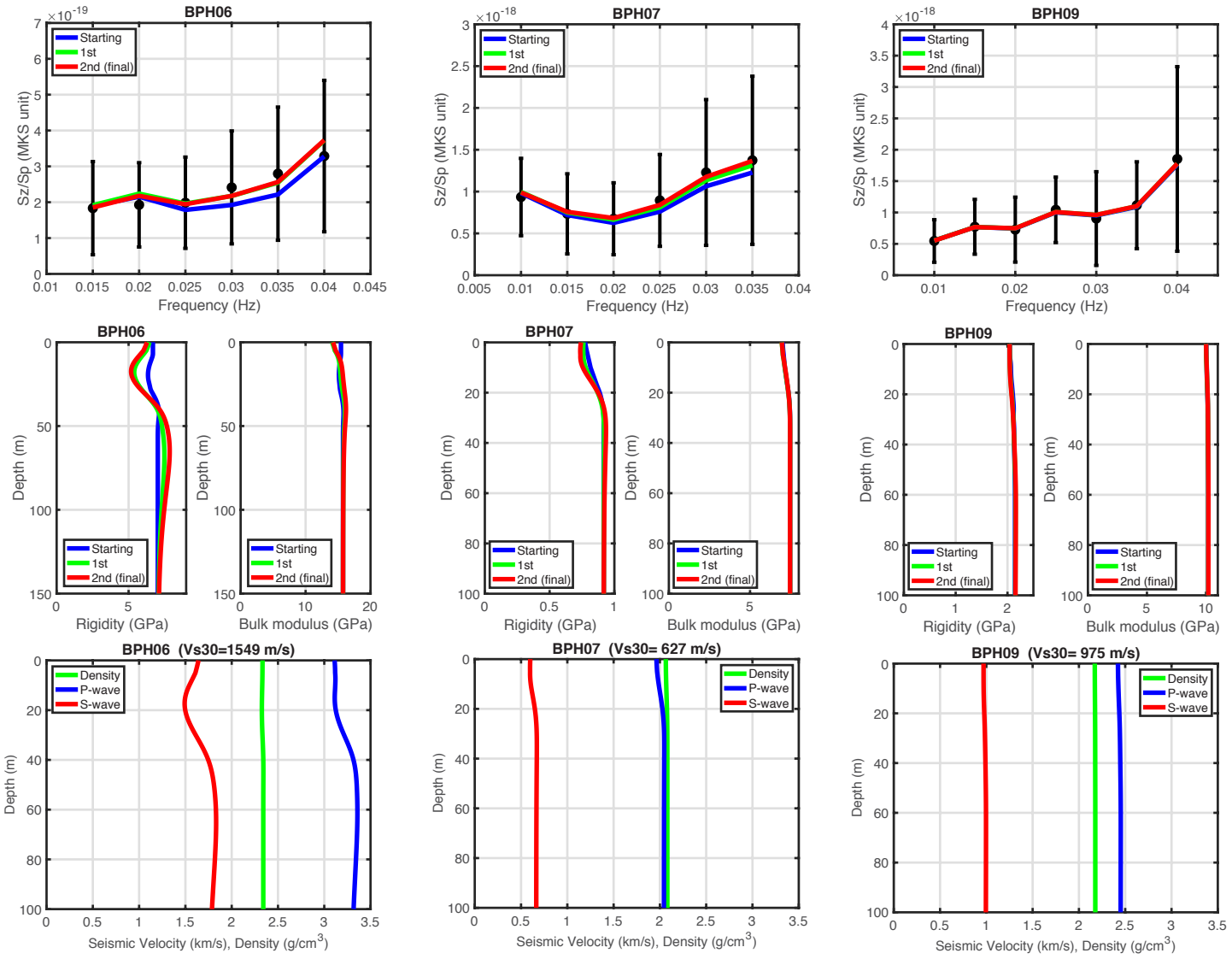

Figure 11: Selected cases of inversion for BPH06 (left), BPH07 (middle) and BPH09 (right). Otherwise, same with Figure 10.

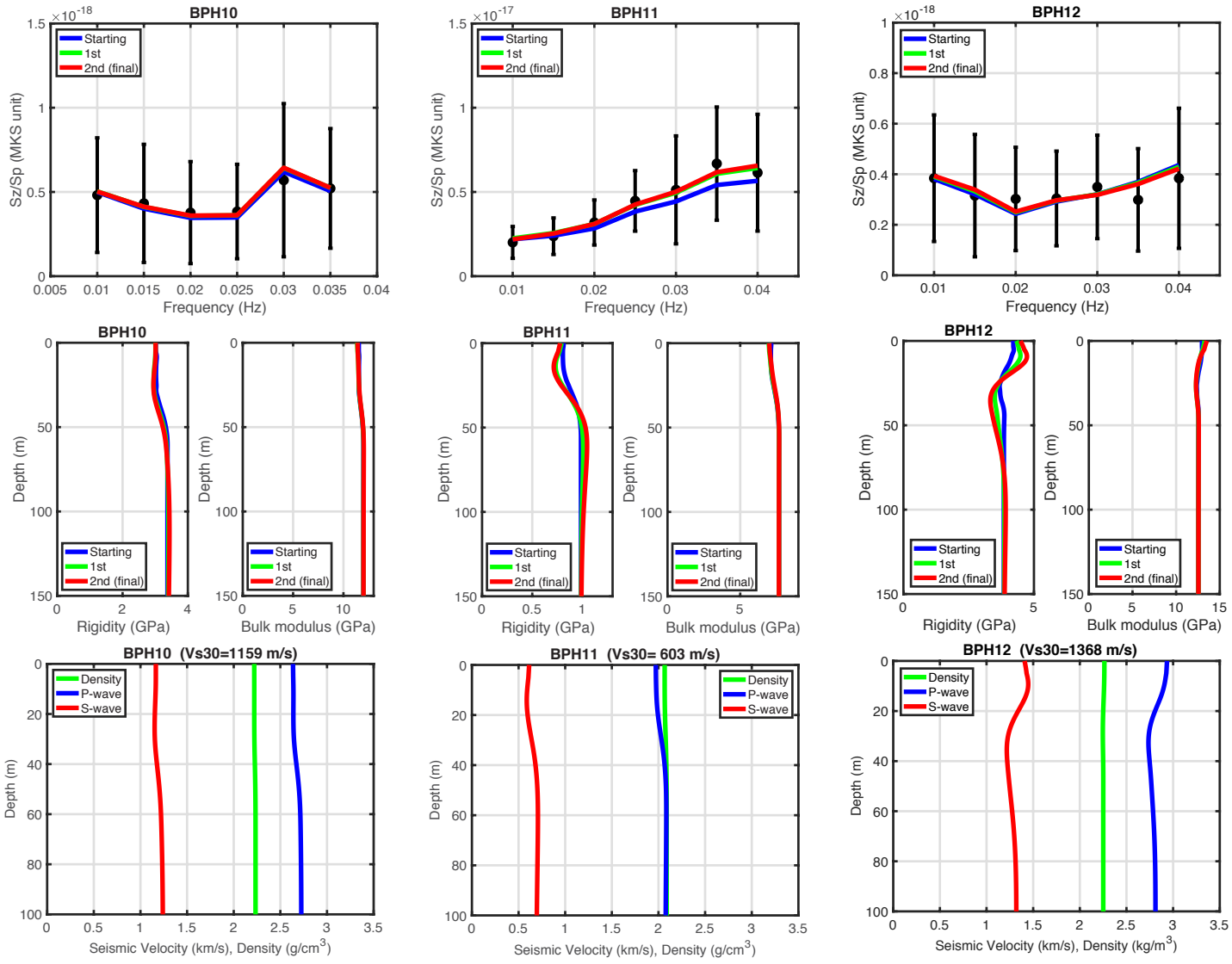

Figure 12: Selected cases of inversion for BPH10 (left), BPH11 (middle) and BPH12 (right). Otherwise, same with Figure 10.

Depth Resolution Kernels

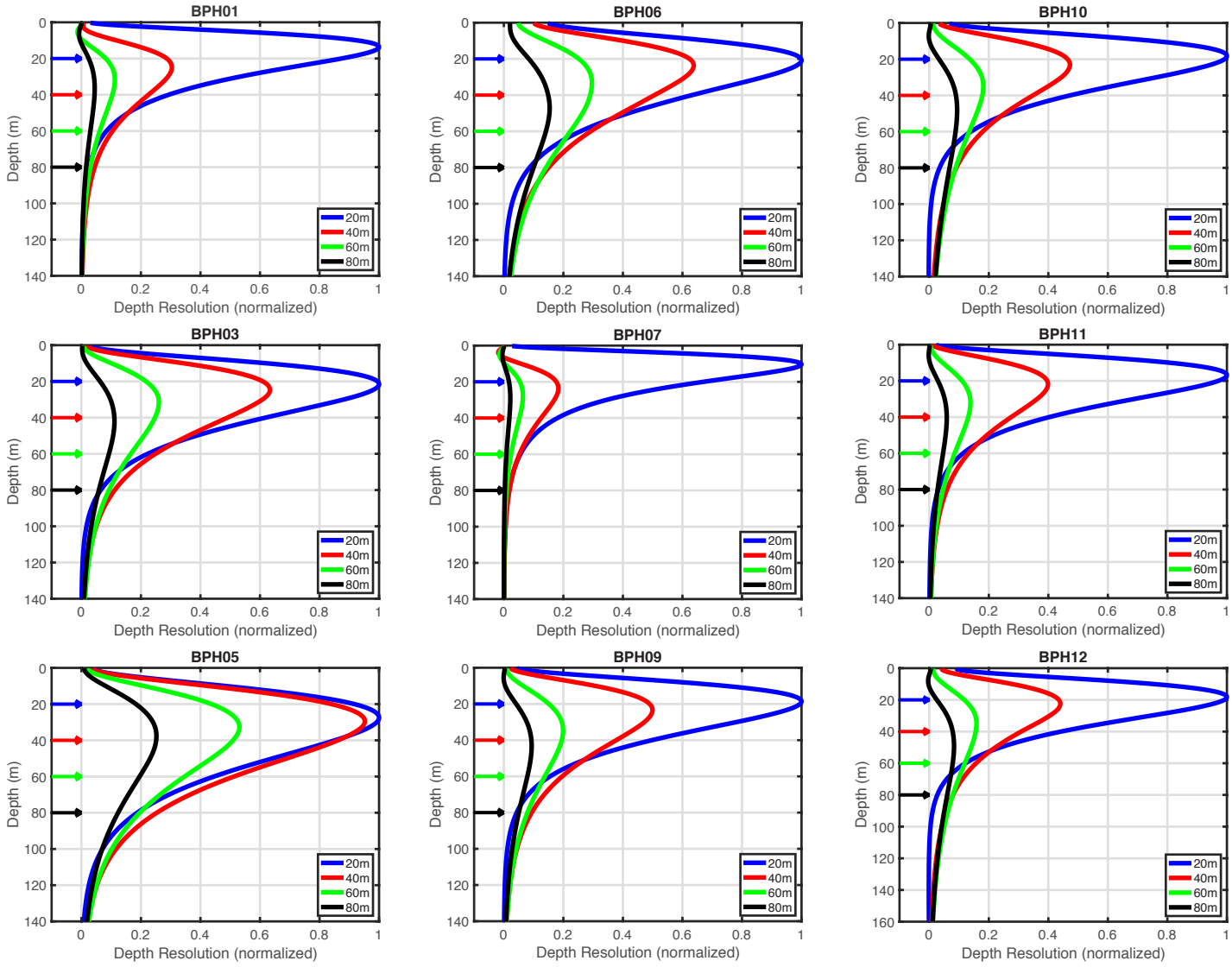

Figure 13: Depth resolution kernels for nine cases of inversions. They correspond to the cases in Figures 10-12.

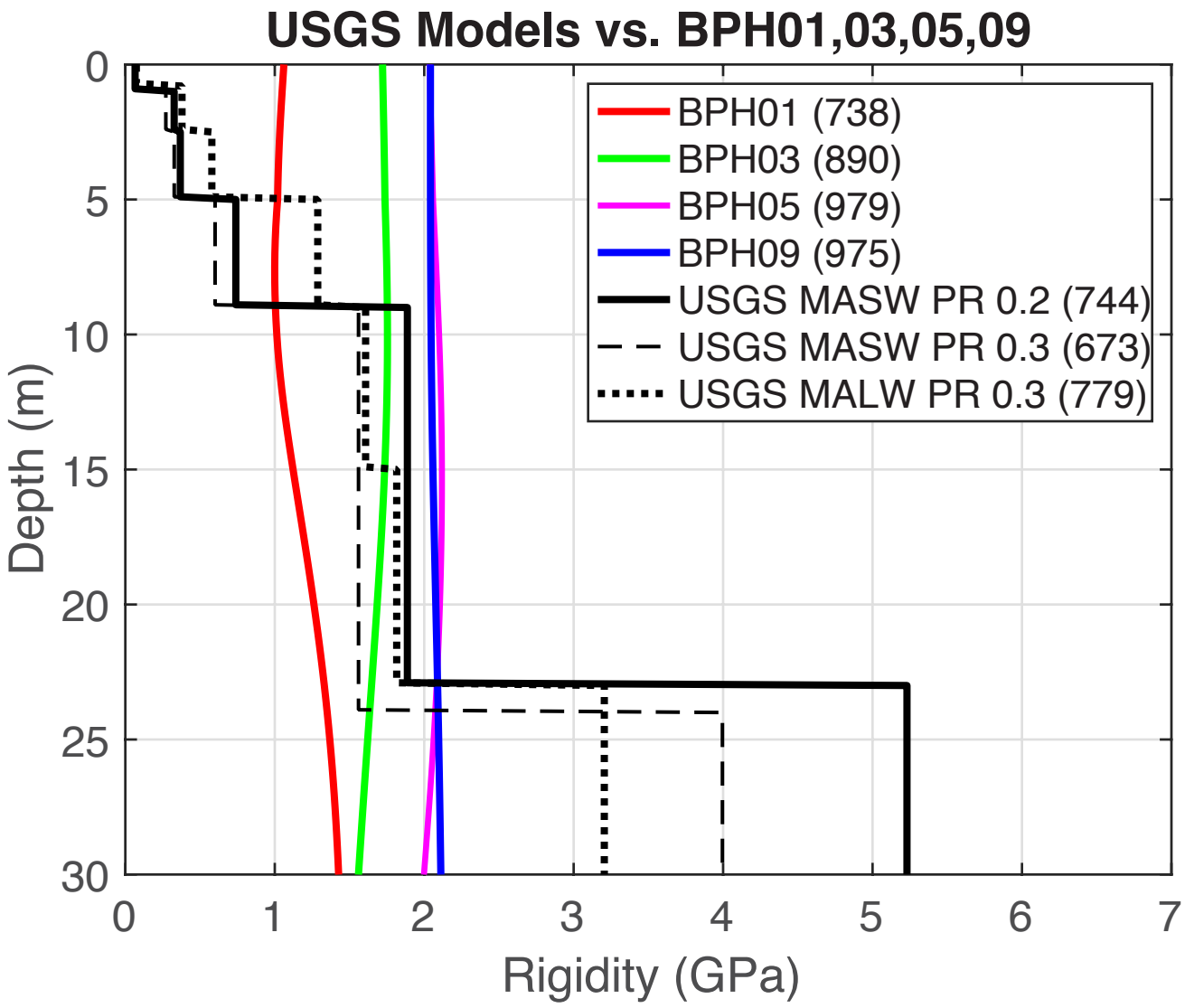

Figure 14: Comparison of the rigidity structures for BPH01, BPH03, BPH05, and BPH09 against three models in Yong et al. (2016). Among their models, two Rayleigh-wave analysis results (MASW, Poisson's ratio 0.2 and 0.3) and one Love-wave analysis results (MALW) are shown. Their models were converted to rigidity structures for comparison. Our results are all very smooth in comparison to their models. Vs30 values are still close, shown in the parentheses in unit of m/s.

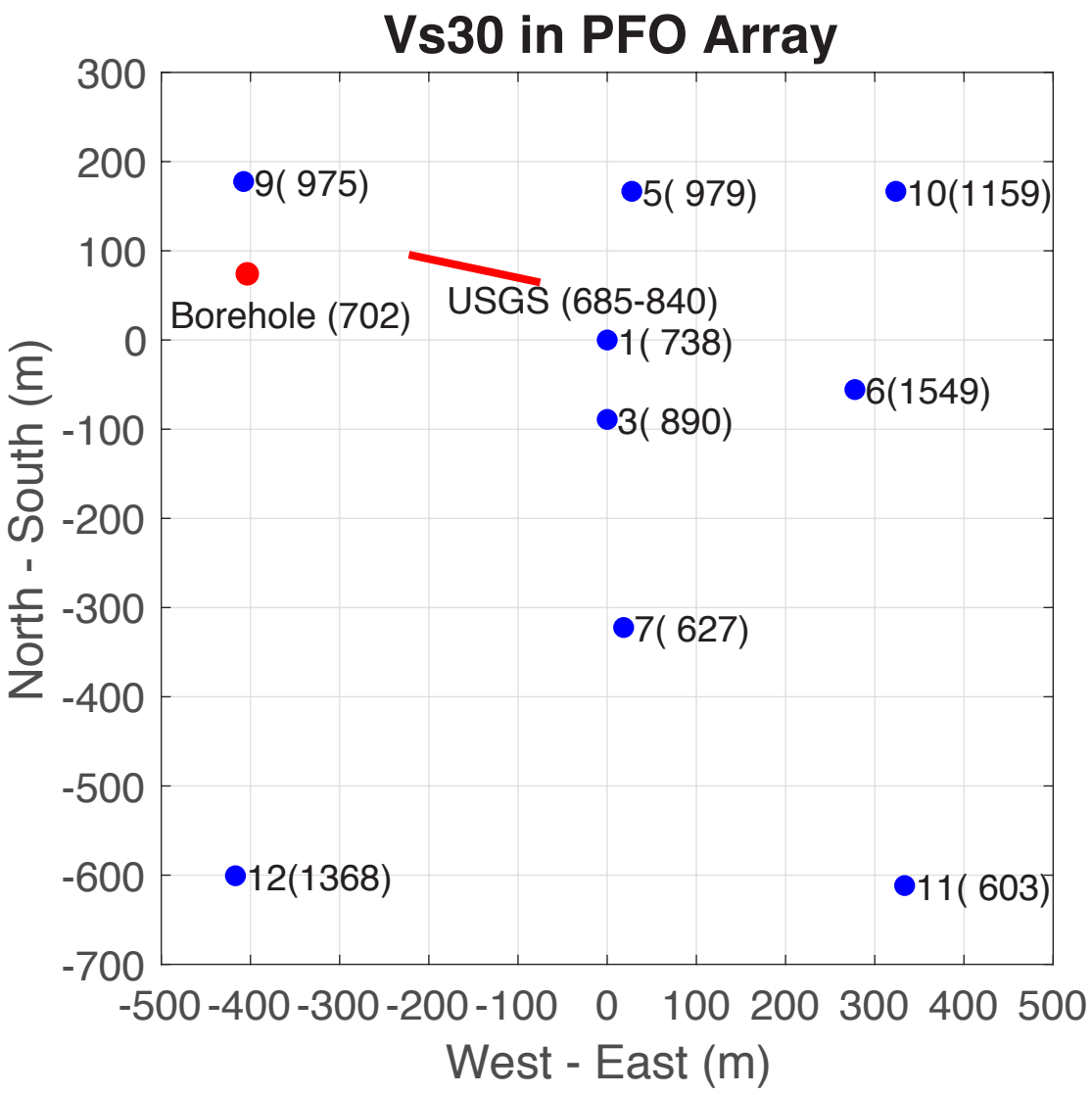

Figure 15: Our estimates of Vs30 for the nine colocated stations compared against Vs30 by Yong et al. (2016) and Vs30 at the borehole based on S-wave speed model in Fletcher et al. (1990). The numbers by blue circles are the station numbers (1 is for BPH01, 3 for BPH03 and so forth). The numbers in parentheses are our estimates for Vs30 in m/s.

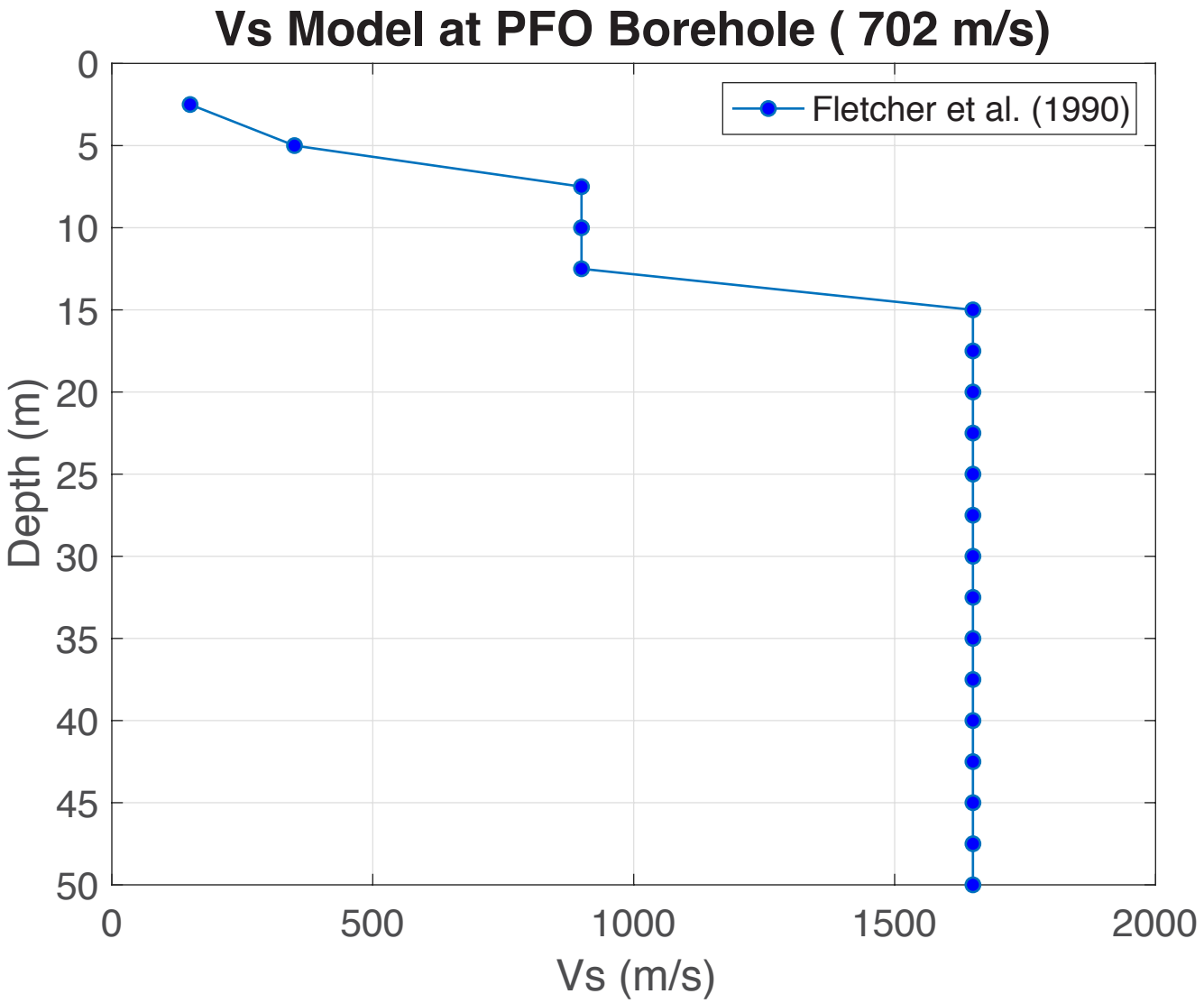

Figure 16: S-wave speed model by Fletcher et al. (1990). Vs30 was computed by integrating this structure in the upper 30 m (Vs30 = 702 m/s).

BPH01

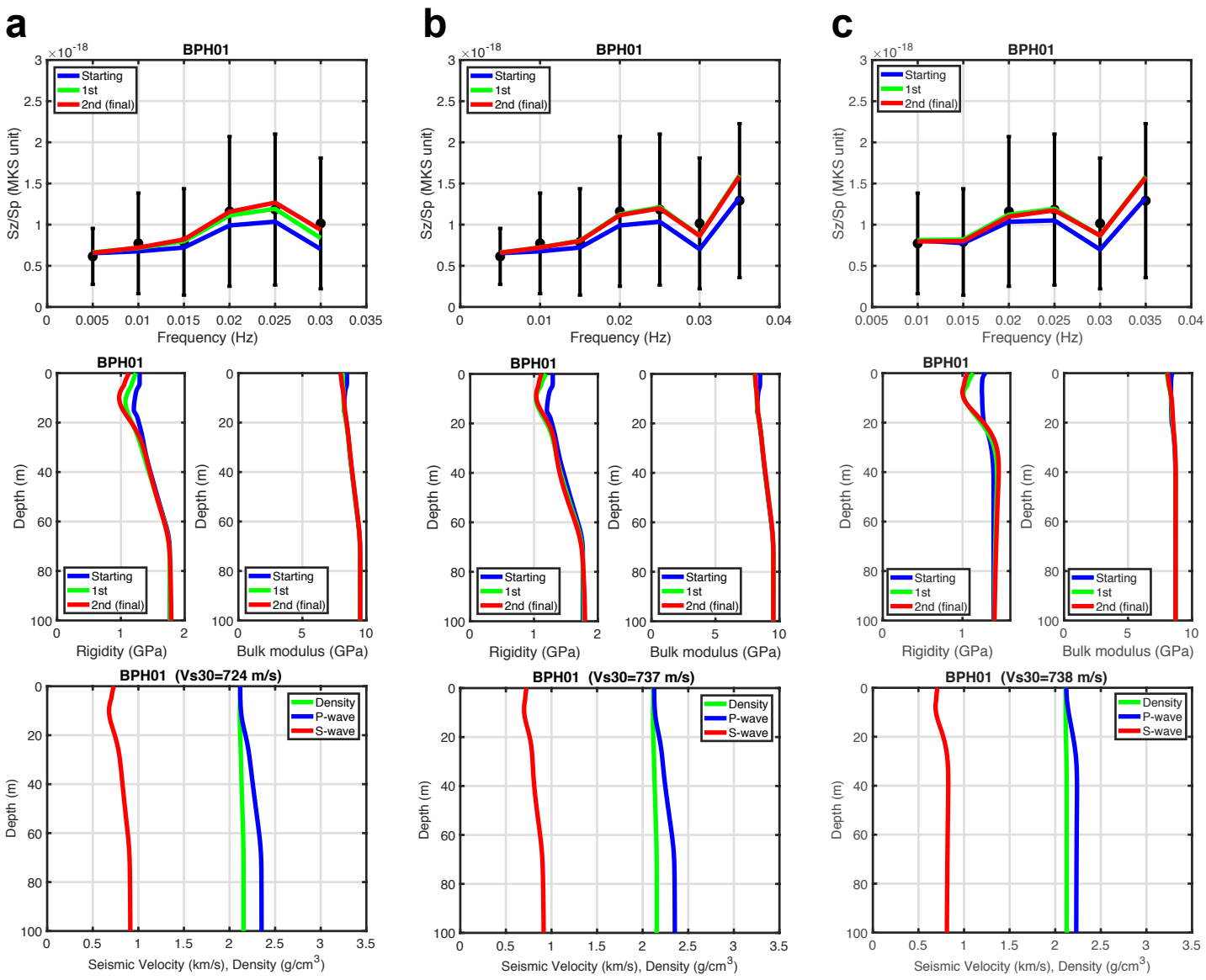

Figure S1: Three cases of inversion for BPH01. The frequency ranges are (a) 0.01-0.035 Hz, (b) 0.005-0.035 Hz, and (c) 0.01-0.04 Hz. Otherwise, same with Figure 10.

BPH03

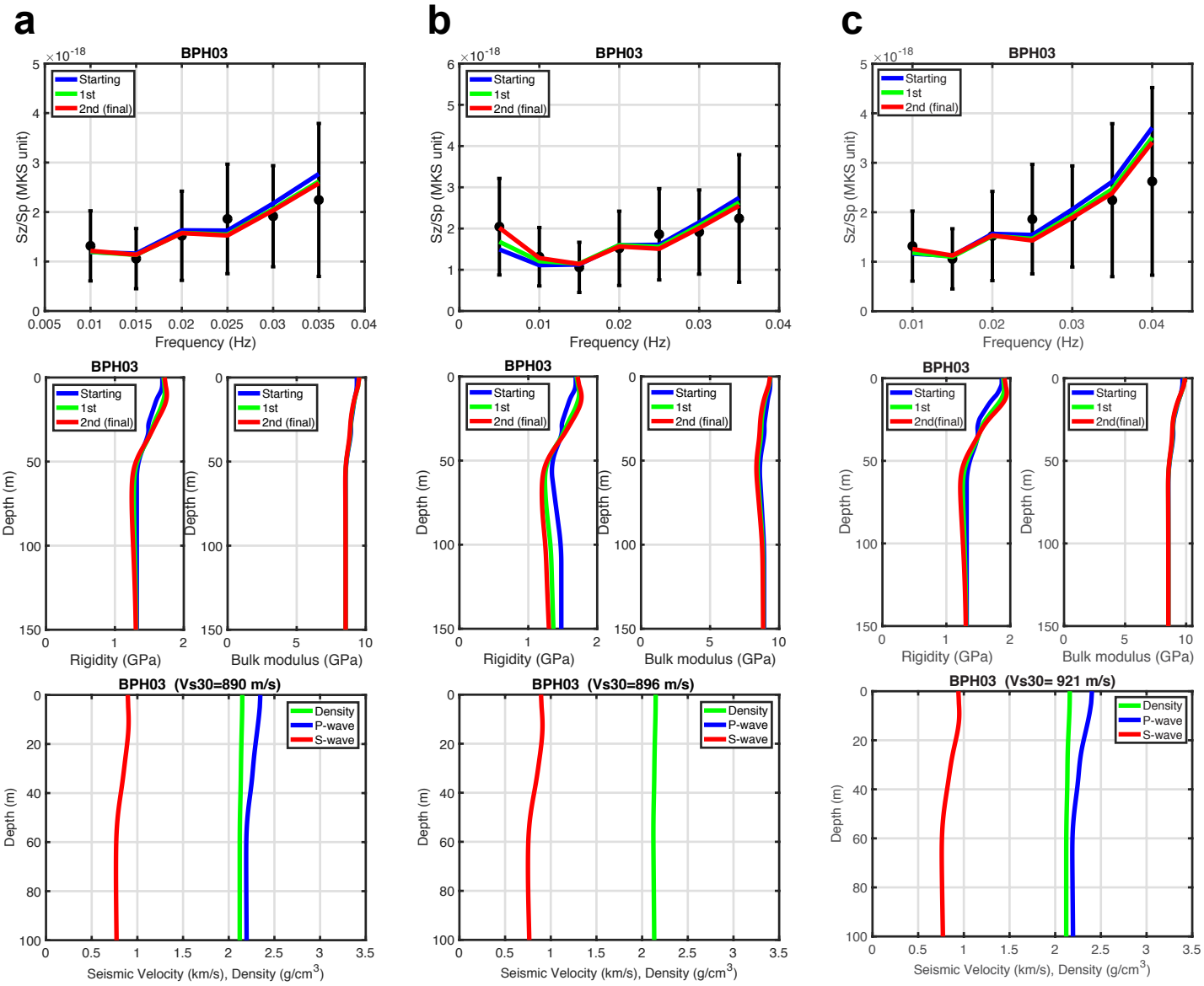

Figure S2: Three cases of inversion for BPH03. The frequency ranges are (a) 0.01-0.035 Hz, (b) 0.005-0.035 Hz, and (c) 0.01-0.04 Hz. Otherwise, same with Figure 10.

BPH05

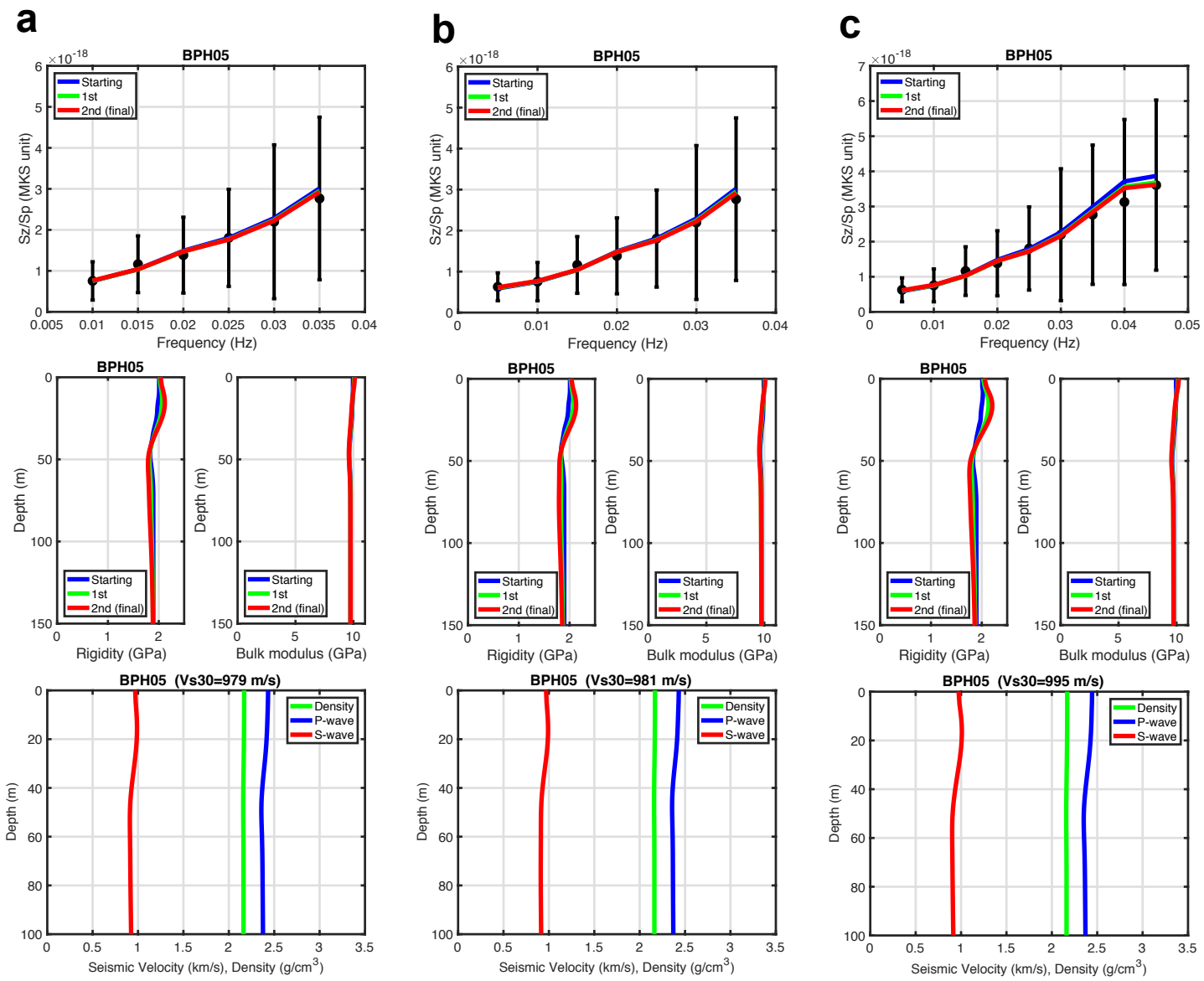

Figure S3: Three cases of inversion for BPH05. The frequency ranges are (a) 0.01-0.035 Hz, (b) 0.005-0.035 Hz, and (c) 0.005-0.045 Hz. Otherwise, same with Figure 10.

BPH06

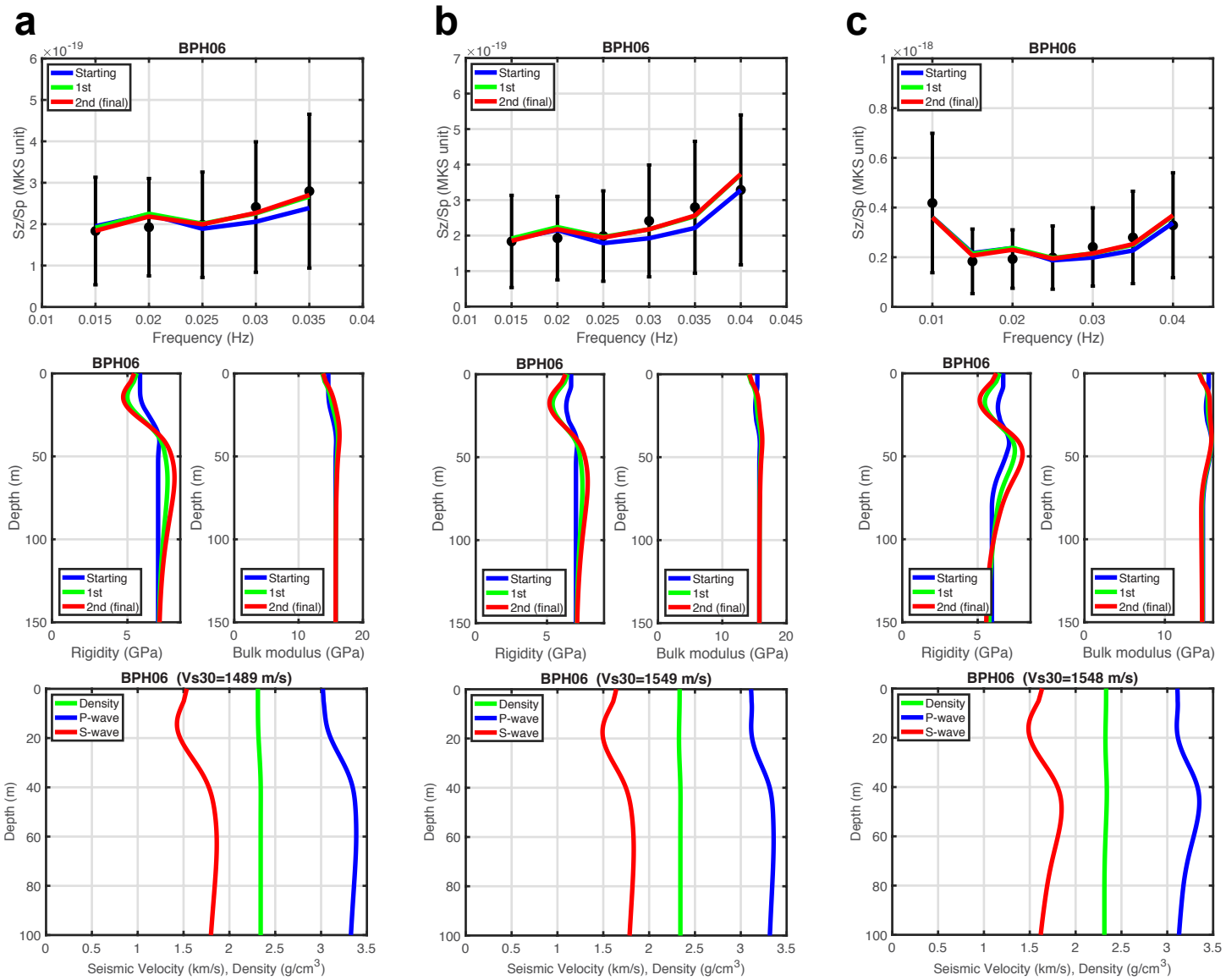

Figure S4: Three cases of inversion for BPH06. The frequency ranges are (a) 0.010-0.035 Hz, (b) 0.015-0.040 Hz, and (c) 0.005-0.040 Hz. Otherwise, same with Figure 10.

BPH07

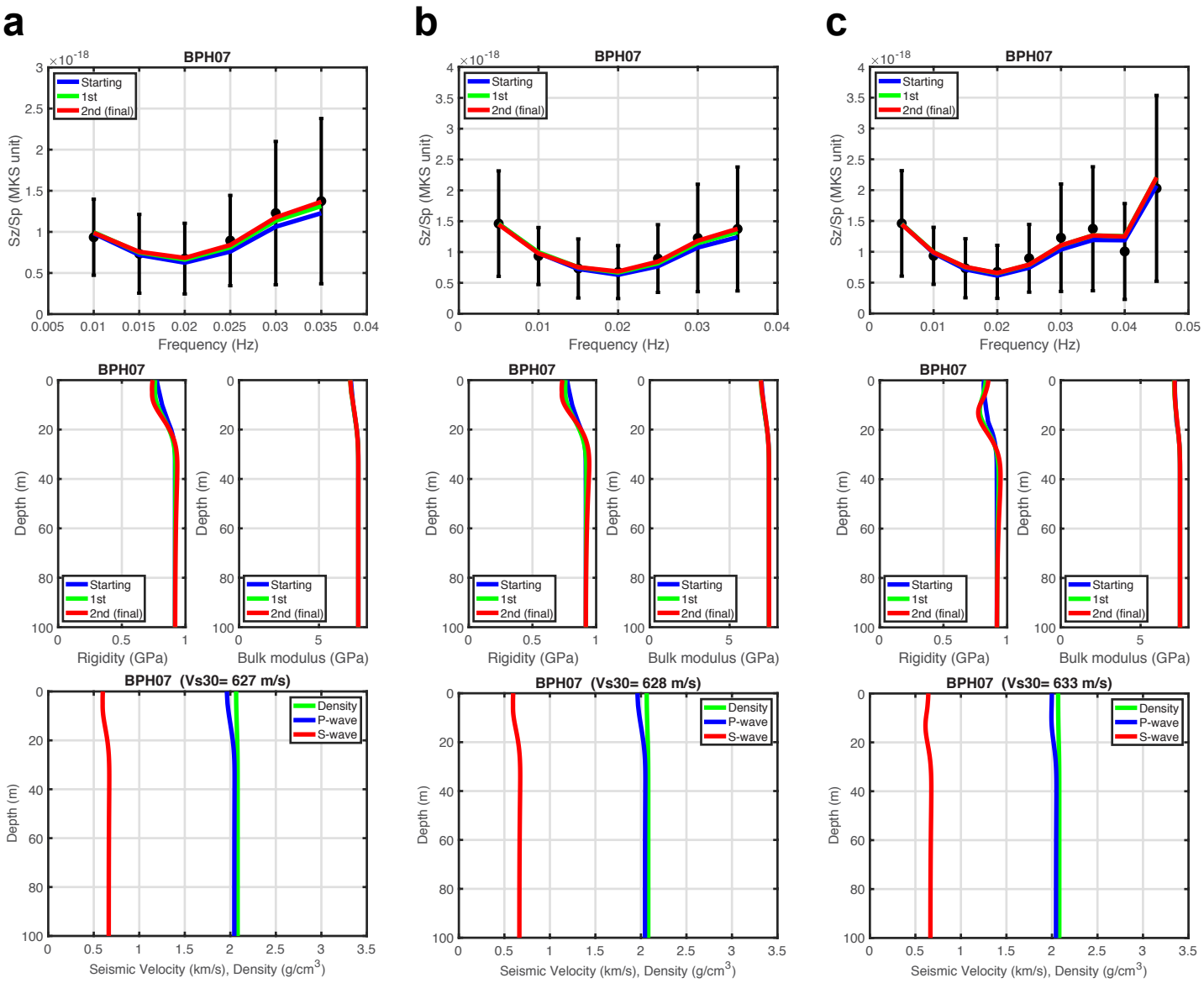

Figure S5: Three cases of inversion for BPH07. The frequency ranges are (a) 0.01-0.035 Hz, (b) 0.005-0.035 Hz, and (c) 0.005-0.045 Hz. Otherwise, same with Figure 10.

BPH09

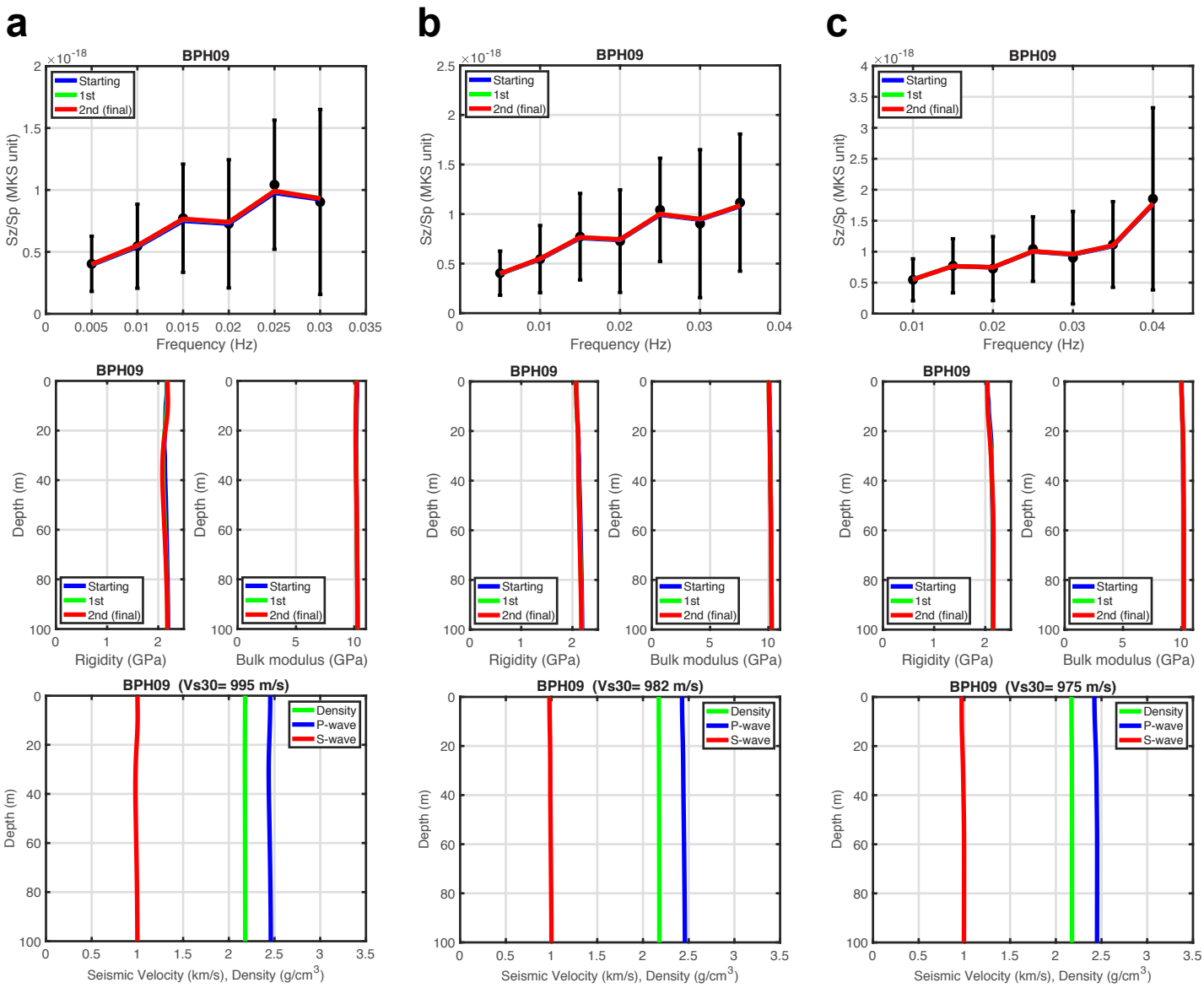

Figure S6: Three cases of inversion for BPH09. The frequency ranges are (a) 0.005-0.030 Hz, (b) 0.005-0.035 Hz, and (c) 0.01-0.04 Hz. Otherwise, same with Figure 10.

BPH10

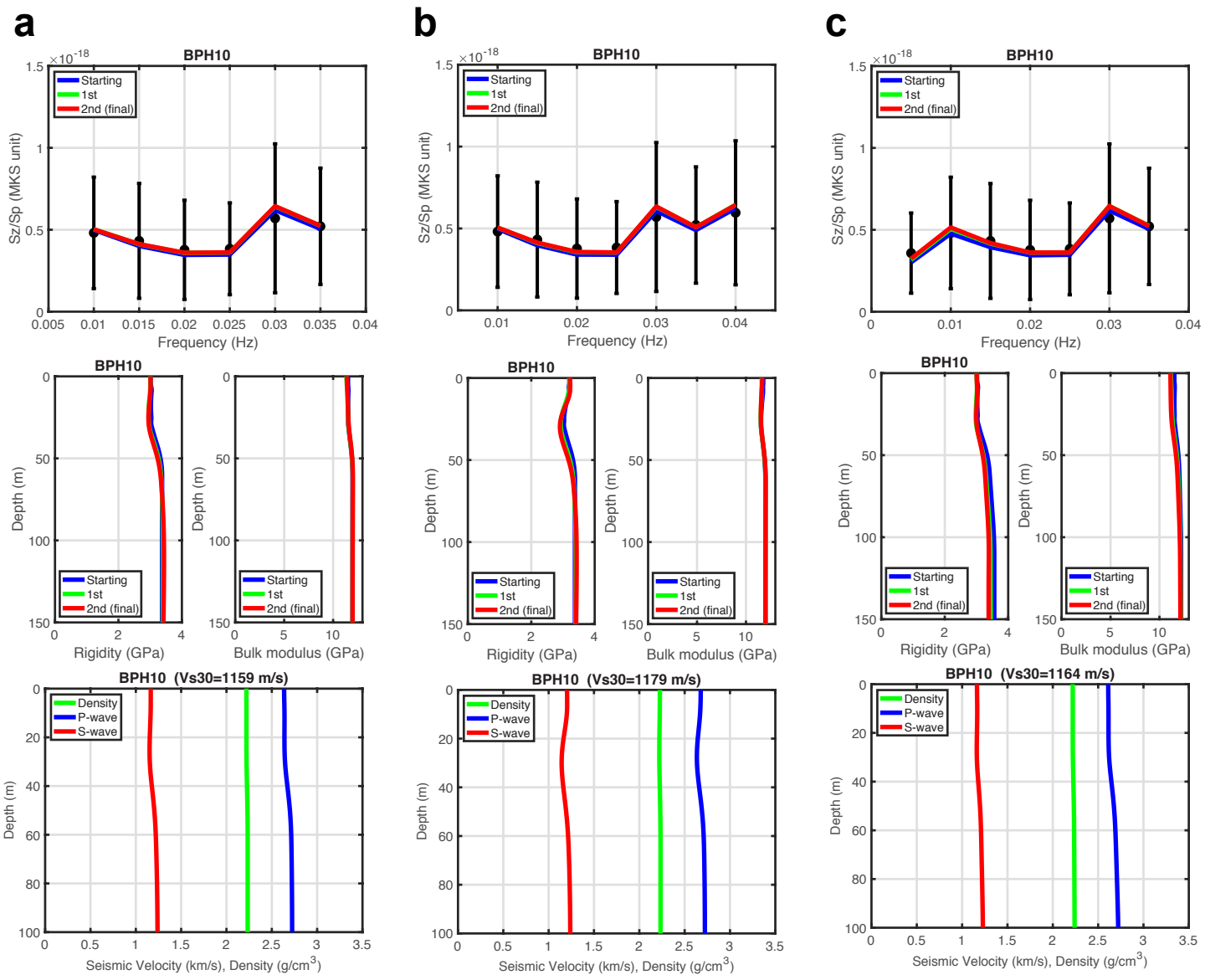

Figure S7: Three cases of inversion for BPH10. The frequency ranges are (a) 0.010-0.035 Hz, (b) 0.010-0.040 Hz, and (c) 0.005-0.035 Hz. Otherwise, same with Figure 10.

BPH11

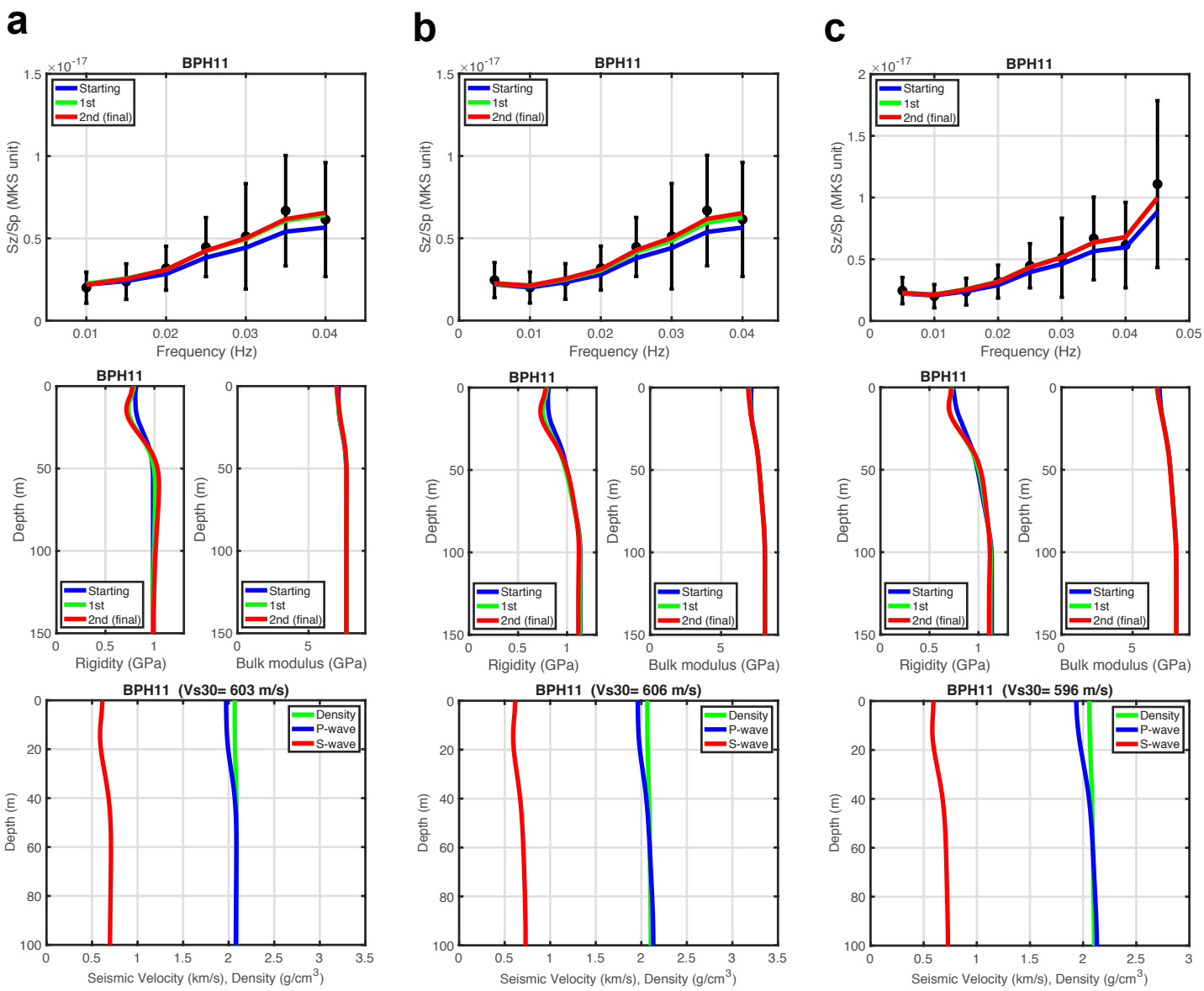

Figure S8: Three cases of inversion for BPH11. The frequency ranges are (a) 0.01-0.040 Hz, (b) 0.005-0.040 Hz, and (c) 0.005-0.045 Hz. Otherwise, same with Figure 10.

BPH12

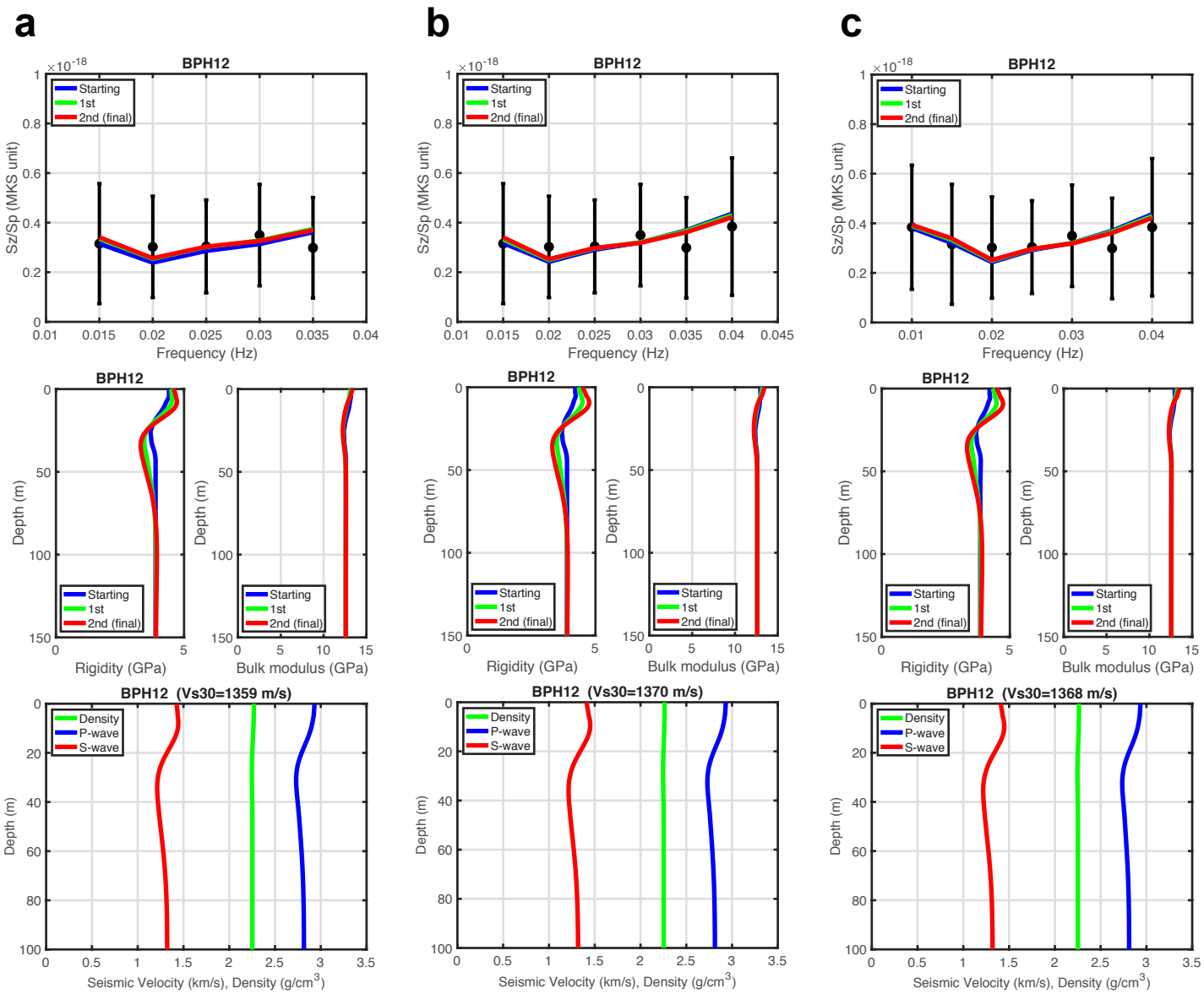

Figure S9: Three cases of inversion for BPH12. The frequency ranges are (a) 0.015-0.035 Hz, (b) 0.015-0.040 Hz, and (c) 0.010-0.040 Hz. Otherwise, same with Figure 10.